ELSEVIER

Journal of Structural Geology 28 (2006) 2237–2258

JOURNAL OF STRUCTURAL GEOLOGY

www.elsevier.com/locate/jsg

Plate motion on Europa and nonrigid behavior of the Icy lithosphere: The Castalia Macula region

G.W. Patterson [a,*], J.W. Head [a], R.T. Pappalardo [b]

[a] *Department of Geological Sciences, Brown University, 324 Brook Street, Providence, RI 02912, USA*
[b] *Laboratory for Atmospheric and Space Physics, University of Colorado, Boulder, CO 80309, USA*

Received 10 August 2005; received in revised form 7 February 2006; accepted 23 March 2006
Available online 24 May 2006

Abstract

We have developed a generalized quantitative technique for determining the finite pole of rotation between two rigid plates and use it to critically examine differing reconstructions of a region surrounding a prominent dark spot on Europa, Castalia Macula. This region is located near the equator of Europa's trailing hemisphere and has been suggested as a site where crustal convergence may have occurred. Previous reconstructions of the region have indicated that a ridge set and/or a band-like complex that define a collection of tectonic plates in the region accommodated surface contraction. However, a critical examination of the differences between these reconstructions has been complicated by the lack of a finite pole of rotation for the plates involved in either reconstruction. We have applied our modeling technique, coupled with a detailed examination of the morphology and cross-cutting relationships involving this ridge set and band-like complex, to determine if a unique reconstruction exists for several tectonic plates in this region. The cross-cutting relationships involving the ridge set also allow us to test the general assumption that plates behave rigidly on Europa. Assuming rigid behavior, our results suggest that a unique reconstruction does exist, indicating the ridge set accommodated surface contraction. However, analysis performed to test the assumption of plate rigidity indicates that one or more of the plates in the region did not behave rigidly. This does not rule out surface contraction along the ridge set but does indicate that a component of nonrigid behavior must be considered.

Keywords: Europa; Compression; Plate rigidity; Inverse modeling; Castalia Macula

1. Introduction and background

Voyager and Galileo spacecraft images of Europa have shown its surface to be extensively disrupted by a multitude of structural features (Fig. 1). Common structural feature types include craters, chaos and lenticulae (also referred to as pits, spots, and domes), ridges, and bands. A comprehensive review of theses types of structural features and the characteristics that distinguish them can be found in Greeley et al. (2004). The present analysis is concerned with two of these structural feature types, ridges and bands. These features appear to form initially as fractures in the brittle lithosphere of Europa that are then modified to produce their present morphology (Schenk and McKinnon, 1989; Pappalardo and Sullivan, 1996; Sullivan et al., 1998; Greenberg et al., 1998; Head et al., 1999; Hoppa et al., 1999a; Prockter et al., 2002; Kattenhorn, 2004). The formation and/or modification of these fractures have been attributed to deformation of the outer ice shell from stresses induced by diurnal tides, nonsynchronous rotation, and/or polar wander (see Greeley et al., 2004 for a review).

Diurnal tides induced by the satellite's orbital eccentricity and its proximity to Jupiter may fracture the ice shell in linear and cycloidal patterns, on the 3.55 day timescale of its orbit (Helfenstein and Parmentier, 1983; Greenberg et al., 1998; Hoppa et al., 1999a,b). Evidence also suggests that the decoupled outer shell of Europa undergoes nonsynchronous rotation due to torques imposed by tidal forces (Greenberg and

* Corresponding author. Tel.: +1 401 863 3485; fax: +1 401 863 3978.
E-mail address: gerald_patterson@brown.edu (G.W. Patterson).

0191-8141/$ - see front matter © 2006 Elsevier Ltd. All rights reserved.
doi:10.1016/j.jsg.2006.03.032

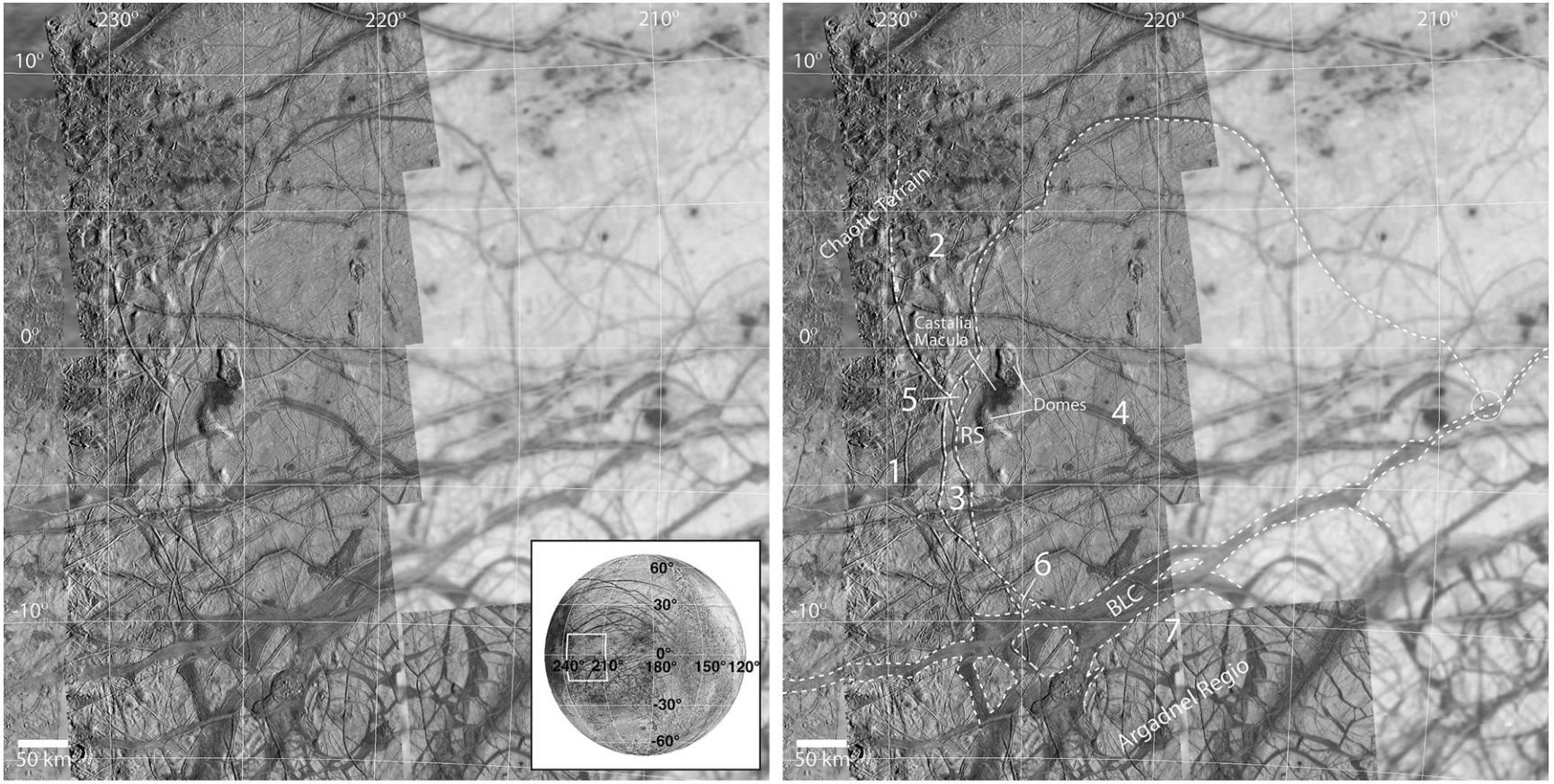

Fig. 1. (a) Image of the region surrounding Castalia Macula taken from the USGS controlled photomosaic of Europa, with inset map showing location of the image on Europa's equatorial trailing hemisphere. The resolution of the mosaic ranges from 220 m/pixel (left) to 1.45 km/pixel (right). (b) Dashed lines indicate possible plate margins outlined by a band-like complex (BLC) and a ridge set (RS). Plates are numbered 1–7. The intersection of the RS with the BLC along the eastern boundary of plate 4 is indicated by a circle.

Weidenshilling, 1984; Ojakangas and Stevenson, 1989a). This mechanism is supported by the orientations of global-scale surface features (McEwen, 1986; Leith and McKinnon, 1996; Geissler et al., 1998) and by regional-scale mapping efforts, which have observed systematically changing orientations of co-located features with respect to age (Figueredo and Greeley, 2000, 2004; Kattenhorn, 2002). The stresses involved with this mechanism would migrate across the surface on timescales $>10^3$ yr (Greenberg et al., 1998; Hoppa et al., 1999b; Hoppa et al., 2001). Polar wonder has been predicted if ice shell thickness at the poles is significantly greater than that at the equator (Ojakangas and Stevenson, 1989b; Leith and McKinnon, 1996). Based on the distribution of strike-slip features mapped from Galileo images, Sarid et al. (2002) have suggested that polar wander has occurred, displacing a paleo-pole $\sim 30^\circ$ toward Europa's leading hemisphere.

The morphologic characteristics of ridges have been described by Head et al. (1999) using five key observations: (1) they are remarkably consistent in their along-strike linearity, width, and height, (2) they form long linear features in which preexisting structures can sometimes be traced up the outer slopes of the ridges and in other cases appear to be buried, (3) they contain narrow apical zones of small-scale, ridge-parallel faulting, (4) they are sometimes flanked by narrow troughs and ridge-parallel fractures, and (5) often display associated color variations.

Greeley et al. (2000) suggest that ridges are the dominant surface feature on Europa and define them in broad terms based on shared morphologic characteristics. They suggest that ridges can range in width from ~ 200 m to >4 km, can be short or can exceed 1000 km in length, and are as high as 200–350 m. They classify ridges as including features that are straight, curvilinear, or cycloidal and forming single ridges, doublet ridges (two ridges separated by a trough), or ridge complexes consisting of more than two ridges. They suggest that ridge complexes can form from anastomosing and discontinuous sets of ridges. This particular ridge type (referred to as complex ridges) has been interpreted to form by merging or successive buildup of ridges and ridge pairs (Figueredo and Greeley, 2000).

Several models have been proposed for the formation of ridges on Europa. These include incremental buildup by wedging (Turtle et al., 1998), compression along fractures (Sullivan et al., 1998), upwarping through linear diapirism (Head et al., 1999), or accumulation through cryovolcanic processes (Kadel et al., 1998). Cross-cutting relationships and the cycloidal nature of some ridges have also led to a model of ridge formation resulting from tidal deformation of the Europa's icy lithosphere (Hoppa et al., 1999a,b; Nimmo and Gaidos, 2002; Marshall and Kattenhorn, 2005). In this model, motion along fractures resulting from rotating diurnal tidal stresses causes strike-slip offsets to develop (Hoppa et al., 1999a). It has been proposed that the motion along these fractures should lead to localized frictional heating that results in upwarping of the surface around the fracture (Nimmo and Gaidos, 2002).

Bands on Europa are commonly recognized by a distinct albedo (typically low) and texture with respect to the surrounding terrain, though they generally appear to brighten with age (Greeley et al., 1998). Figueredo and Greeley (2000) identified two primary types of band material: smooth band material and ridged band material. The first is characterized by generally linear, curvilinear, or cuspate features bound by single, moderate-relief ridges at their margins. The interior of this type of band consists of either very subdued ridges and troughs or material with little or no structure. The second band material type is characterized by linear to curvilinear features consisting of alternating ridges and troughs oriented subparallel to the band margins. Ridged bands generally have parallel margins but rarely present bilateral symmetry. Both of these morphologies were interpreted to have formed by separation of the crust of Europa along fractures and infilling by material from below (Figueredo and Greeley, 2000).

Several distinct morphologic characteristics, observed in association with some bands, have also been discussed in detail by Prockter et al. (2002). These include the presence of interior linear structures subparallel with the band margins, a central trough that tends to be axially symmetric to the band margins, and a region of hummocky texture that can be isolated and symmetric with the axial trough or span the width of the band. These characteristics were used to suggest that Europan bands may form by processes analogous to terrestrial mid-ocean ridges (Prockter et al., 2002).

Not all bands analyzed by Prockter et al. (2002) share all of these characteristics. There are observed variations in morphology from one band to another, and Prockter et al. (2002) suggested that this may be a result of differences in rates of formation. Notably, bands that lack prominent axial troughs and are composed of a uniformly small-scale hummocky-textured material (bands C and E from Prockter et al., 2002) may suggest rapid formation of the band, where newly formed material did not thicken until it was well off the axis of symmetry.

The formation of bands and ridges on Europa create offsets of preexisting structural features that cross their boundaries. The successful reconstruction of preexisting offset structural features along a number of bands and ridges has led to the general conclusions that the lithosphere of Europa behaves rigidly and that it is broken into plates that rotate with respect to one another (e.g., see Schenk and McKinnon, 1989; Sullivan et al., 1998; Nimmo and Gaidos, 2002). Using this assumption, numerous additional reconstructions of Europa's tectonically disrupted surface have been performed (e.g., Tufts et al., 1999, 2000; Pappalardo and Sullivan, 1996; Sarid et al., 2002; Patterson and Pappalardo, 2002; Prockter et al., 2002; Greenberg, 2004; Kattenhorn, 2004). With the exception of Schenk and McKinnon (1989) and Pappalardo and Sullivan (1996), each of these reconstructions was performed using a planar approach.

A planar approach assumes the features that are being reconstructed (and the plates they define) on the surface of the satellite lie on a flat plane. This assumption is valid when attempting to reconstruct small areas of the surface where the curvature of the body is negligible. However, when reconstructing large areas of the surface, significant errors can be introduced when using this method and it becomes necessary

to perform reconstructions on a sphere instead. Determining a finite pole of rotation is a convenient means of describing the relative motion between rigid plates on a sphere and this is a commonly determined quantity when describing plate motions on Earth (e.g., McKenzie and Parker, 1967; Chase, 1978; DeMets et al., 1990; Dixon et al., 1996; Mikhail et al., 2000). A finite pole of rotation is a quantity that describes the rotation of two rigid plates relative to each other on a sphere by a scalar angle about a pivot point (an Euler pole). All rigid plate motions on a sphere are describable by finite rotations.

We have developed a generalized quantitative technique for determining the finite pole of rotation between two rigid plates and use it here to gain insight into the nature of deformation of Europa's lithosphere. This is an inverse modeling technique that uses an iterative grid-search method to test a wide range of possible rotation poles for the reconstruction of a two-plate system in which one plate has been displaced relative to another. The reconstruction of this system about the best-fit pole determined by this technique represents the best approximation of the previous position of the plates prior to deformation. The uniqueness of the determined pole for a two-plate system using this technique relies on the assumption that the plates involved behaved rigidly during deformation. This technique can also be used to reconstruct multi-plate systems, if they can be confidently subdivided into a collection of two-plate systems.

We apply this method to determine if a unique reconstruction exists for a region on Europa surrounding the prominent dark spot Castalia Macula (Fig. 1). The cross-cutting relationships of a ridge set (RS) and a band-like complex (BLC) suggest the region can be divided into seven major plates that cover $\sim 20^\circ$ lat. $\times\, 20^\circ$ lon. of the equatorial trailing hemisphere of Europa (Fig. 1b). Planar reconstructions of some of these plates have been attempted previously, suggesting that one or both of the structural feature types that comprise their boundaries may have accommodated surface contraction (Patterson and Pappalardo, 2002; Sarid et al., 2002). However, those reconstructions, and where they indicate surface contraction was accommodated, differ significantly. We will discuss the differences between these previous reconstructions in more detail in the following section.

In the following analysis, we examine in detail the morphology of the structural features that comprise the boundaries of this system of plates, and their cross-cutting relationships with each other and the surrounding terrain. We then use the inverse modeling technique we have developed to attempt to reconstruct the region. We do this with two principal questions in mind: (1) can ridges and/or bands accommodate surface contraction; and (2) is our assumption of plate rigidity on Europa valid?

2. Geologic setting

The prominent dark spot, Castalia Macula, is located near the equator of Europa's trailing hemisphere (2°S and 226°W) and is surrounded by a diverse assemblage of structural features (Fig. 1b). Our analysis will focus on a ridge set (RS) and band-like complex (BLC) found in this region, and each will be described in detail below. Both of these features have been proposed as possible sites where compression has been accommodated by the loss of surface material (Patterson and Pappalardo, 2002; Sarid et al., 2002). These conclusions were drawn from inferences about the morphology of these two features and planar reconstructions of offset preexisting linear features along the RS. However, significant differences exist between these two reconstructions and the manner in which they were performed makes it difficult to directly compare them and critically examine which (if either) of the reconstructions is accurate. If the RS and BLC represent the margins of a system of rigid plates, then the application of our inverse modeling technique can resolve this issue by providing a statistically quantifiable and reproducible reconstruction of these features.

For context and analysis of the morphology and cross-cutting relationships of the RS and BLC, we consider the region surrounding Castalia Macula from $\sim 15^\circ$S to 15°N and from 235°W to 205°W (Fig. 1a and b). This area was imaged by the Galileo spacecraft at a resolution of 1.45 km/pixel during the E14 encounter, and portions of it were imaged again at a regional-scale resolution of 220 m/pixel during the E17 encounter. The image data of Fig. 1 are from the USGS controlled photomosaic of Europa, in a transverse Mercator projection about 227°W. All subsequent images, and all location measurements cited in this work, are obtained from a Mercator projection of an image mosaic of the 220 m/pixel data (Europa_pole_2_pole01.cub), produced by the University of Arizona's Planetary Image Research Laboratory.

Prominent structural features observed in this region include chaotic terrain to the northwest, Argadnel Regio to the southeast, several large domes (including two associated with Castalia Macula), a number of E–W to SW–NE trending bands and band-like features, and numerous ridges and complex ridges with no apparent preferred orientation. Among these structures, we have mapped (Fig. 2) the extent of the RS and BLC within the regional resolution coverage (220 m/pixel) along with a number of other prominent bands and ridges that both pre- and post-date the RS.

2.1. The ridge set (RS)

We define the RS as a collection of ridges that represent a single through-going structure that formed in a series of events. The RS trends predominately N–S in the regional resolution coverage (220 m/pixel) of the Castalia Macula region (Fig. 1b) with one portion arcing to the east and then to the south. The interpretation of the RS as a single through-going structure is based on spatial interrelationships of the ridges that comprise the RS and cross-cutting relationships of those ridges with respect to the surrounding terrain. The series of events that formed the RS can be inferred through the cross-cutting relationships of the ridges that comprise it.

The ridges that comprise the RS have a generally typical double ridge morphology, as defined in the previous section. However, there are two anomalous morphological characteristics associated with the RS that are noteworthy. The first is an alternating transition from a double ridge morphology to

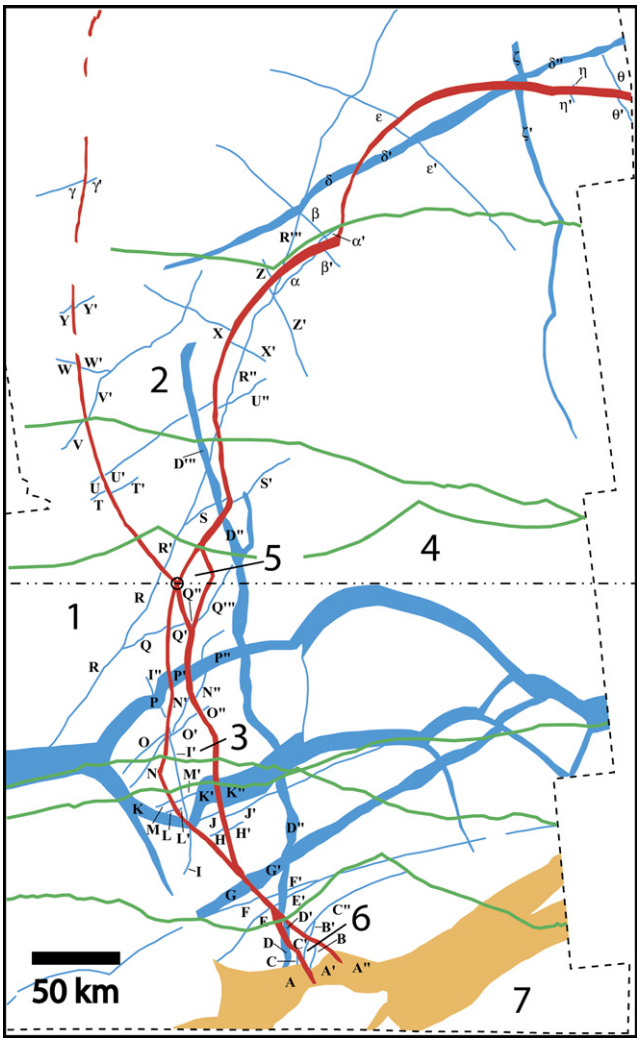

Fig. 2. Sketch map of region surrounding Castalia Macula from ~10°S to 11°N lat. and ~218°W to 232°W lon. The RS and BLC are shown in red and orange, respectively. Features inferred to pre-date the formation of the RS and BLC are blue, and features that post-date them are green. Offset pre-existing features are designated A–Z and α–θ, with a prime (′) added for each time a feature is significantly offset from east to west. Dashed line indicates boundary of regional-scale (220 m/pixel) image coverage in this region. Dash-dot-dot horizontal line and open circle indicate locations of arbitrary plate boundary and a point, respectively, used in determination of the amount of distributed deformation in this multi-plate system.

a band morphology and back (Fig. 3a), where one of the ridges traces a cycloidal path through the region (Fig. 1b). This characteristic may be the result of tailcrack formation proceeded by dilation in response to dextral strike-slip motion along N–S trending portions of the ridge (Kattenhorn, 2004). The second anomalous characteristic is the presence of a hummocky medial trough up to several kilometer in width along portions of the ridges instead of a V-shaped axial trough (Fig. 3b). This characteristic remains unexplained.

The ridges that comprise the RS overlap and intersect each other at 8.5°S, 225°W, 7.7°S, 226°W, and again at three locations within a ~30 × 50 km region centered around 2°S, 227°W (Fig. 1b). Fig. 4 shows this last region, and we use the intersections there to determine the cross-cutting relationships of these ridges with respect to each other. We interpret these relationships to suggest that the ridges that comprise the RS formed in three distinct events. This interpretation is supported by the cross-cutting relationships of the other two ridge intersections of the RS. We use the terminology RS_1, RS_2, and RS_3, respectively, when alluding to these events.

The sequence of events that formed the RS and how each of these events affected various ridges that comprise the RS are illustrated in Fig. 5. From Fig. 5d we can see that, while some portions of the RS were only active during RS_1, RS_2, or RS_3, many portions of the RS were active during some combination of RS_{1-3}. These spatial relationships are consistent with the interpretation that the ridges involved can be classified as a single feature that formed in three phases.

The interpretation that the RS represents a single through-going structure is further supported by the cross-cutting relationships of the ridges that comprise RS with respect to the surrounding terrain. The RS offsets a number of preexisting ridges, complex ridges, and bands. In Figs. 2 and 5 we have mapped 34 of the more prominent of these offset structural features observed in the regional resolution coverage of the region surrounding Castalia Macula. Six of these preexisting features are wide enough that offsets could be measured from each edge of the feature (D, G, K, P, δ, and ζ) and 11 of the preexisting features are offset by the RS more than once (A, C, D, K, P, O, N, Q, R, U, and δ). This results in a total of 60 measurable offsets of preexisting structural features along the RS (Table 1).

To illustrate how the cross-cutting relationships of the ridges that comprise the RS with respect to the surrounding terrain indicate the ridges are related, we use observations of preexisting linear features that are offset by the RS more than once and linear features that post-date the formation of the RS. Ten of the 11 preexisting features identified as being offset by the RS more than once were offset by more than one of the events inferred to have formed the RS (δ is the exception). In every case the ridges that comprise the RS post-date these features. There are also six east–west trending ridges that cross and overlap the ridges that comprise the RS (Fig. 2). In this case, five of these younger ridges overlap ridges of the RS that were active during some combination of the events that formed the RS. In each of these cases, the ridges post-date all of the portions of the RS they cross.

Having established that the RS appears to represent a single through-going structure, we examine the cross-cutting relationships of the RS with the surrounding terrain to get a sense of the style of deformation that resulted in its formation. The presence of offsets along the RS suggests formation via strike-slip motion. In Table 1 we list the locations of the 60 observed offsets along the RS (Fig. 2) using three points; A_i, B_i, and C_i. Also listed are the magnitudes of those offsets, with negative values representing sinistral offsets. These magnitudes are measured utilizing two methods.

The measured offset (d_m) is determined using the distance between the two intersections of a preexisting offset linear feature along the RS. These intersections are represented by

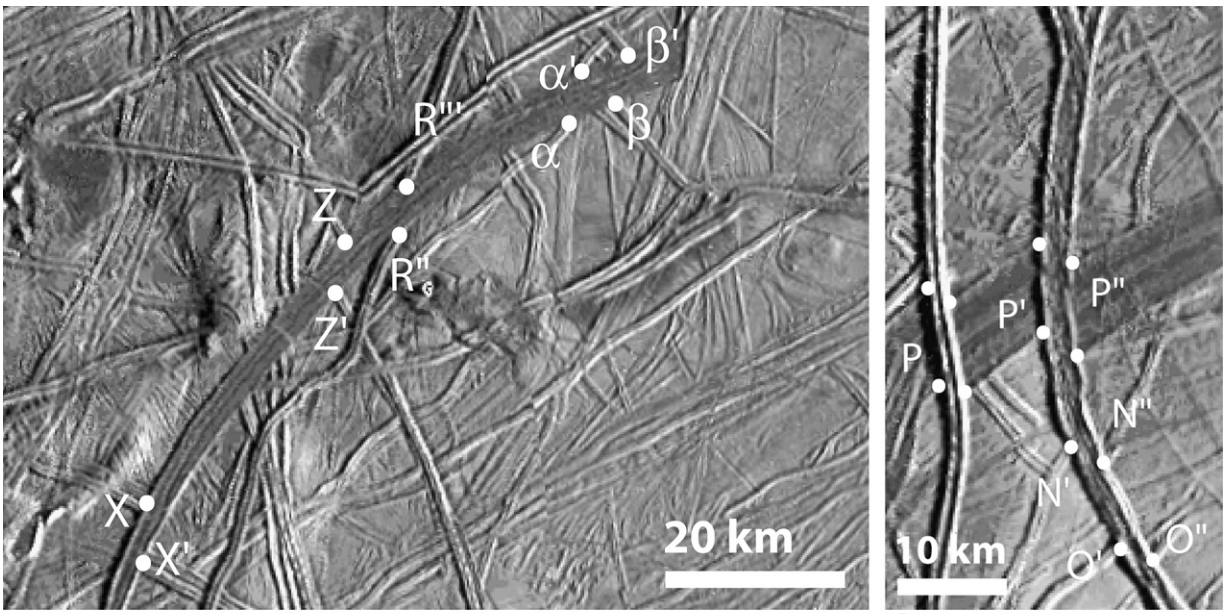

Fig. 3. Images highlighting various morphologies within the RS. Prominent preexisting offset linear features along the ridges are marked in correspondence with Fig. 2. (a) Portions of the RS have a morphology that is more characteristic of bands. (b) The western ridge in this image fits the description of a typical double ridge with a v-shaped axial trough. However, the eastern ridge contains a hummocky medial trough several kilometer in width that is not characteristic of ridges.

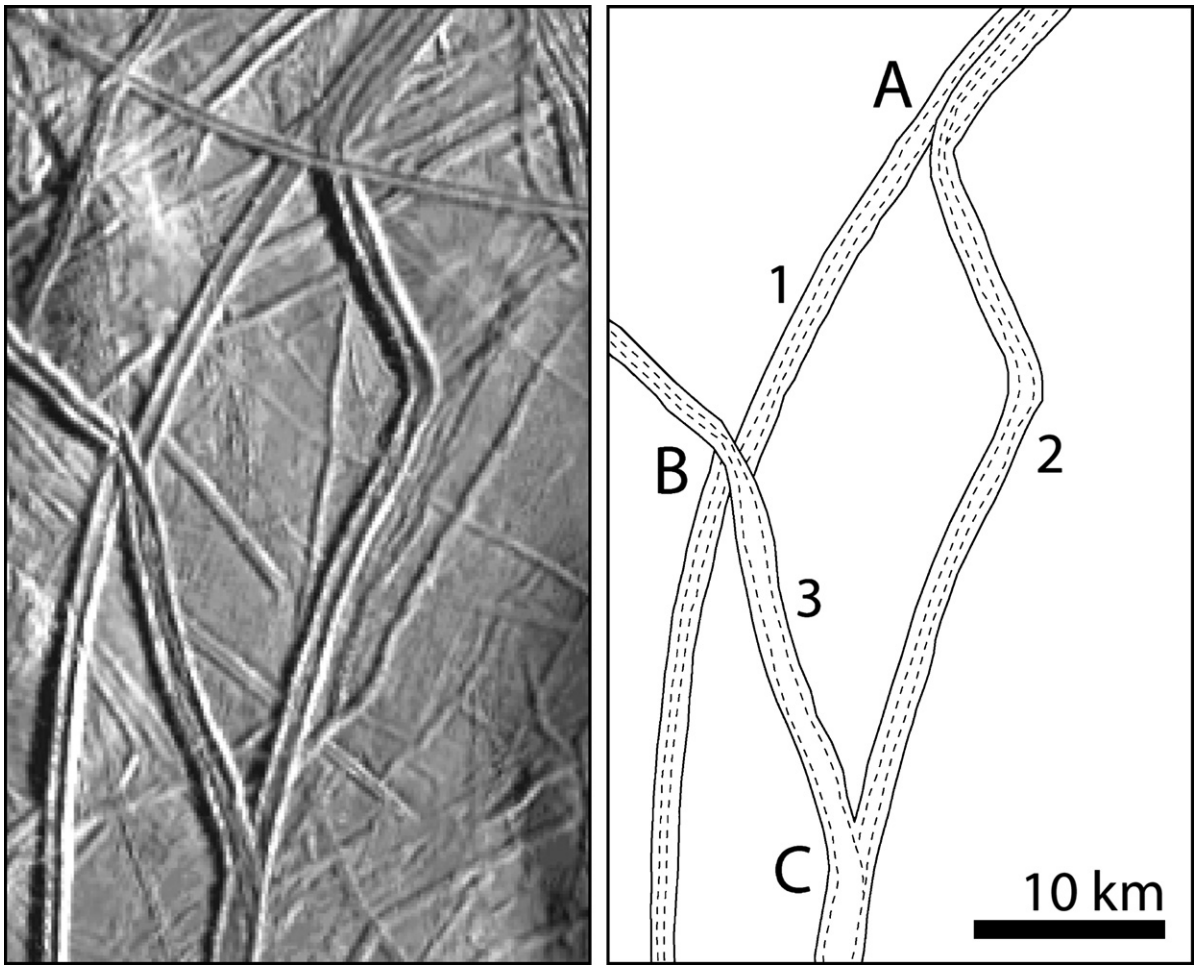

Fig. 4. Image and sketch map of the margins of a 30 × 50 km region centered at 2°S, 227°W (Fig. 1) illustrating the sequence of formation of the ridge set. Intersections of ridges within the RS are labeled A−C and the ridges themselves are labeled 1−3 in the order we propose that they formed (oldest to youngest, respectively). That interpretation is as follows: ridge 1 is overlapped by ridge 2 at intersection A, ridge 1 is overlapped and offset in a right-lateral sense by ridge 3 at intersection B, and ridge 2 is overlapped by ridge 3 at intersection C.

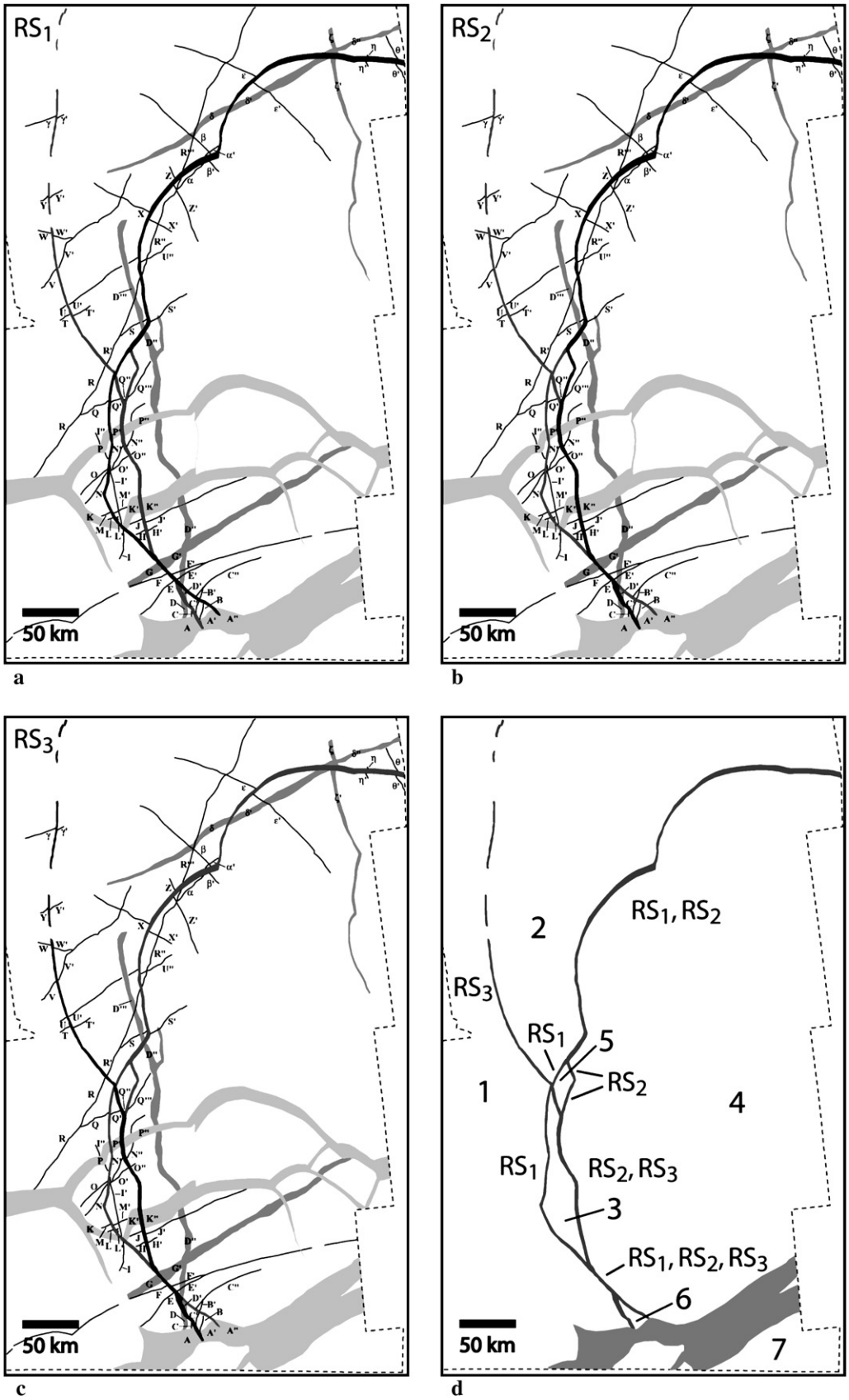

Fig. 5. Sketch maps illustrating the sequence of ridge formation indicated by Fig. 4. (a)–(c) Sketch maps of RS_{1-3}, each corresponding to an inferred event in the formation of the RS. For each event illustrated, active features are shown in black and inactive features are shown in gray. (d) Corresponding labels summarize which portions of the RS were active during the formation of RS_1, RS_2, and/or RS_3, as suggested by (a)–(c). The RS and BLC are shown in gray, and plates defined by these features are numbered 1–7.

Table 1

Feature ID	Morphologic type	Locations for model inputs along offset linear features on fixed plate				Location of model input for corresponding offset linear features on plate to be rotated (C_i)		Measured offset − d_m (km)	Calculated offset − d_c (km)
		Starting Lat./Lon. (A_i)		Ending Lat./Lon. (B_i)					
A–A′	Band	−9.742	225.078	−9.642	224.740	−9.796	224.654	4.3	4.6801
A′–A″		−9.606	224.390	−9.382	224.175	−9.412	224.133	1.5	1.3913
B–B′	Ridge	−9.415	224.529	−9.181	224.509	−9.124	224.637	−4.0	−3.5737
C–C′	Ridge	−9.670	224.900	−9.414	224.884	−9.564	224.769	6.2	3.3255
C′–C″	Ridge	−9.253	224.692	−9.121	224.631	−9.039	224.750	−4.2	−3.8488
D_e–D'_e	Complex ridge	−9.319	225.104	−9.154	225.106	−9.231	225.064	3.4	1.0999
D_w–D'_w		−9.235	225.225	−8.883	225.220	−8.978	225.171	3.6	1.3597
D'_e–D''_e	Complex ridge	−8.946	225.071	−8.782	225.087	−8.660	225.195	−4.5	−2.5714
D'_w–D''_w		−8.856	225.182	−8.661	225.185	−8.566	225.28	−4.6	−2.6416
E–E′	Ridge	−8.631	225.617	−8.461	225.419	−8.498	225.375	1.4	1.5310
F–F′	Ridge	−8.398	225.876	−8.283	225.609	−8.326	225.571	1.6	1.4786
G_s–G'_s	Complex ridge	−8.217	225.982	−8.102	225.780	−8.136	225.75	1.7	1.2601
G_n–G'_n		−8.017	226.210	−7.866	225.983	−7.900	225.951	1.4	1.2453
H–H′	Ridge	−6.956	226.556	−6.845	226.364	−6.919	226.339	2.0	2.0814
I–I′	Ridge	−7.084	227.155	−6.762	227.157	−6.725	227.203	−2.2	−1.2573
J–J′	Ridge	−6.621	226.748	−6.500	226.439	−6.633	226.395	3.6	3.7933
K_s–K'_s	Band	−6.844	227.352	−6.879	227.008	−6.831	227.053	−1.8	−1.1815
K_n–K'_n		−6.589	227.577	−6.665	227.262	−6.632	227.283	−1.5	−0.73287
K'_s–K''_s	Band	−6.368	226.727	−6.303	226.479	−6.439	226.445	4.1	3.8105
K'_n–K''_n		−5.815	226.801	−5.747	226.566	−5.876	226.529	3.7	3.6702
L–L′	Ridge	−6.541	227.629	−6.445	227.420	−6.492	227.396	1.3	1.4212
M–M′	Ridge	−6.430	227.669	−6.325	227.493	−6.380	227.451	2.0	1.8608
I′–I″	Ridge	−4.898	227.533	−4.519	227.620	−4.593	227.627	3.3	0.63435
N–N′	Ridge	−5.182	227.746	−4.947	227.583	−5.026	227.583	2.9	1.2263
O–O′	Ridge	−5.048	227.781	−4.890	227.581	−5.023	227.579	3.3	2.7222
N′–N″	Ridge	−4.619	227.162	−4.447	226.909	−4.518	226.860	4.0	2.3540
O′–O″	Ridge	−4.244	227.199	−4.059	227.079	−4.109	226.986	3.0	2.8460
P_s–P'_s	Band	−4.009	227.629	−3.905	227.507	−3.982	227.491	2.2	1.8710
P_n–P'_n		−3.737	227.749	−3.576	227.556	−3.669	227.541	2.4	2.2053
P'_s–P''_s	Band	−3.878	227.359	−3.703	227.137	−3.832	227.076	3.7	3.8101
P'_n–P''_n		−3.561	227.396	−3.376	227.122	−3.533	227.110	3.7	3.7412
Q–Q′	Ridge	−2.823	227.717	−2.676	227.556	−2.795	227.545	2.6	2.6053
Q′–Q″	Ridge	−2.686	227.316	−2.629	227.144	−2.691	227.122	1.9	1.7897
Q″–Q‴	Ridge	−2.684	227.117	−2.667	227.010	−2.619	226.993	−1.5	−1.2185
R–R′	Ridge	−1.693	227.740	−1.498	227.706	−1.545	227.658	2.2	1.5080
S–S′	Ridge	−0.139	226.498	−0.013	226.295	−0.139	226.252	3.2	3.5469
R′–R″	Ridge	1.036	226.674	1.423	226.538	1.389	226.517	2.3	0.85991
T–T′	Ridge	0.024	228.966	0.099	228.790	0.015	228.750	2.0	2.5293
U–U′	Ridge	0.262	229.072	0.414	228.923	0.330	228.891	2.1	2.2364
U′–U″	Ridge	2.996	226.591	3.183	226.311	2.903	226.342	5.3	5.8831
V–V′	Ridge	1.413	229.388	1.567	229.258	1.488	229.226	2.0	2.0654
W–W′	Ridge	2.710	229.657	2.661	229.407	2.604	229.398	1.8	1.4672
X–X′	Ridge	3.466	226.437	3.349	226.212	3.146	226.295	6.1	5.9660
Y–Y′	Ridge	3.784	229.688	3.897	229.537	3.832	229.524	1.5	1.6450
Z–Z′	Ridge	4.582	225.548	4.372	225.419	4.216	225.502	4.0	4.1806
R″–R‴	Ridge	5.112	225.068	4.467	225.313	4.476	225.258	−4.9	−1.3259
γ–γ′	Ridge	6.348	229.566	6.453	229.298	6.385	229.300	1.6	1.7582
D''_w–D'''_w	Complex ridge	−0.848	226.398	−0.500	226.557	−0.461	226.524	1.7	1.2560
D''_e–D'''_e		−0.664	226.281	−0.375	226.476	−0.310	226.442	1.6	1.7694
α–α′	Ridge	5.294	224.391	5.175	224.500	4.951	224.550	−1.5	−3.0941
β–β′	Ridge	5.436	224.462	5.109	224.170	5.040	224.340	5.8	4.7260
δ_s–δ'_s	Complex ridge	6.426	224.191	6.752	223.627	6.668	223.507	3.0	3.6105
δ_n–δ'_n		6.787	223.802	6.930	223.516	6.825	223.575	3.2	1.8532
ε–ε′	Ridge	8.112	223.598	7.705	222.737	7.550	222.899	6.6	5.7154
δ'_s–δ''_s	Complex ridge	8.569	220.043	8.326	220.672	8.271	220.491	−6.2	−3.1845
δ'_n–δ''_n		8.617	220.289	8.310	220.961	8.311	220.790	−4.0	−1.9186
ζ_e–ζ'_e	Complex ridge	8.90	220.282	8.313	220.101	8.266	220.222	3.3	3.5072
ζ_w–ζ'_w		8.725	220.343	8.314	220.241	8.316	220.372	3.5	3.4167
η–η′	Ridge	8.375	219.159	8.298	219.120	8.172	219.212	3.9	3.7548
θ–θ′	Ridge	8.891	218.513	8.100	218.115	8.085	218.248	4.8	3.3946

Subscripts e, w, n, and s are used to denote which margin of a feature that a location is taken from when the distance between the margins of a feature allows for z measurements to be made (i.e., with complex ridges and bands).

the points B_i and C_i. This method determines the true offset along the plate boundary and we use it when drawing comparisons between the preexisting offset linear features we have identified.

The calculated offset (d_c) is determined by measuring the perpendicular distance from one intersection of a preexisting offset linear feature along a plate boundary (represented by the point C_i) to a plane formed by the trend of the corresponding intersection of the same preexisting offset linear feature across the plate boundary. The plane is determined using the points A_i and B_i. This method of determining offset magnitude is used in our numerical modeling technique. Further explanation of this method will be provided in the next section.

A graphical representation of the offset magnitudes determined by these two methods is provided in Fig. 6. From this figure, we can see that the offsets of 25 of the 34 preexisting linear features we have identified along the RS suggest it generally accommodated dextral strike-slip motion. However, nine examples of sinistral offset of preexisting features along the RS are also identified, and the magnitude of offset for preexisting features ranges from ~1.3 to 6.6 km. These characteristics suggest a deformation history for the RS that is more complex then simple strike-slip motion.

Based on our analysis of the temporal and spatial relationships of the ridges, one explanation for the observed characteristics of the preexisting offset linear features could be the result of different portions of the ridges having experienced different combinations of events RS_{1-3} (Fig. 5d). For example, one portion of the RS may have only been affected by RS_1 and offset by x km as a result, another portion by RS_2 and offset by y km, and still a third portion by RS_1 and RS_2 and, therefore, offset by $x+y$ km. Each scenario would result in a different offset magnitude for the preexisting features involved.

This hypothesis can be tested by grouping the offsets of preexisting structural features along the RS based on which event(s) (RS_1, RS_2, and/or RS_3) they were actively accumulating slip. If variations in offset magnitude are simply the result of variations in the number of events during which a given preexisting feature accumulated slip, then consistent offset magnitudes should be observed within the groupings. Based on Fig. 5d, we have subdivided the RS into five groups: features offset by RS_1; by RS_1 and RS_2; by RS_2 and RS_3; by RS_3; and by RS_1, RS_2, and RS_3. RS_2 was excluded as a group because only one of the features we have identified (Q″–Q‴ in Figs. 2 and 5) was affected solely by that event. The offset magnitudes of preexisting linear features along the RS and within these groups are shown in Fig. 7. Among these five groups of preexisting offset linear features along the RS, only Fig. 7d and e appear to have consistent offset magnitudes (vary by <1 km from feature to feature). This suggests that variations in the offset magnitude and direction of preexisting linear features along the RS cannot be explained solely by variations in the number of events during which a given preexisting feature accumulated slip.

Two other possible explanations for the observed characteristics of preexisting features along the RS are: (1) ridges associated with the RS accommodated some degree of compression, and/or (2) the plates involved in the formation of the RS did not behave rigidly. We will use the technique described in Section 3 to test these possibilities.

2.2. The band-like complex (BLC)

The BLC (Figs. 1b and 8) was first described as a distinct feature by Sarid et al. (2002). It trends ENE–WSW for over 800 km across Europa and it has albedo and textural differences with the surrounding terrain that suggest it is morphologically similar to Europan bands. Subdued linear structures present within the margins of the BLC and the absence of an axial trough (Fig. 8a) suggest that, if the BLC were a band and formed via mid-ocean ridge style spreading (Prockter et al., 2002), it may have formed relatively rapidly.

There are some morphological characteristics that appear to distinguish the BLC from Europan bands. For instance, if we view the BLC as a singular feature, the linear structures present within the band are not parallel to the margins of the complex. Furthermore, the boundaries of the complex itself are not parallel. These characteristics do not fit the basic definition of a band, suggesting the BLC may have formed by a process other than crustal extension. In fact, these characteristics were used as part of an argument by Sarid et al. (2002) to suggest that the BLC is not an extensional band but instead represents a region of crustal convergence.

We suggest an alternative explanation for the morphology of this feature based on our examination and interpretation of three characteristics of the BLC. First, there appear to be overlapping relationships present among the linear structures found within the hummocky interior of the BLC (A of Fig. 8a and b). Second, there are ridges that mark the boundary of some portions of the complex and appear to cut and overlap other portions of it (C of Fig. 8a and b). Third, there are also isolated regions of apparent preexisting terrain within the BLC that reinforce these overlapping relationships (B of Fig. 8a and b). These characteristics can be accounted for if we consider the BLC to represent a collection of superposed features rather than a singular one. Using these overlapping relationships we interpret the present configuration of the BLC to be the result of the formation of three superposed features (Fig. 8b). We will henceforth refer to these features as BLC_1, BLC_2, and BLC_3.

Using this interpretation, BLC_1 appears to share morphological characteristics with features observed throughout Argadnel Regio (the ‘‘wedges’’ region of Europa’s trailing hemisphere). These features have been associated with extension and strike-slip motion (Schenk and McKinnon, 1989; Prockter et al., 1999; Schulson, 2002). BLC_2 has parallel, ridge-bounded borders with a subdued interior. These characteristics, coupled with the albedo and texture differences with the surrounding terrain, suggest it is a band. The regions of preexisting terrain at (B) of Fig. 8a may then indicate a bifurcation in the band during its formation. BLC_3 has approximately parallel borders, portions of which are ridge-bounded, and a subdued interior. These characteristics,

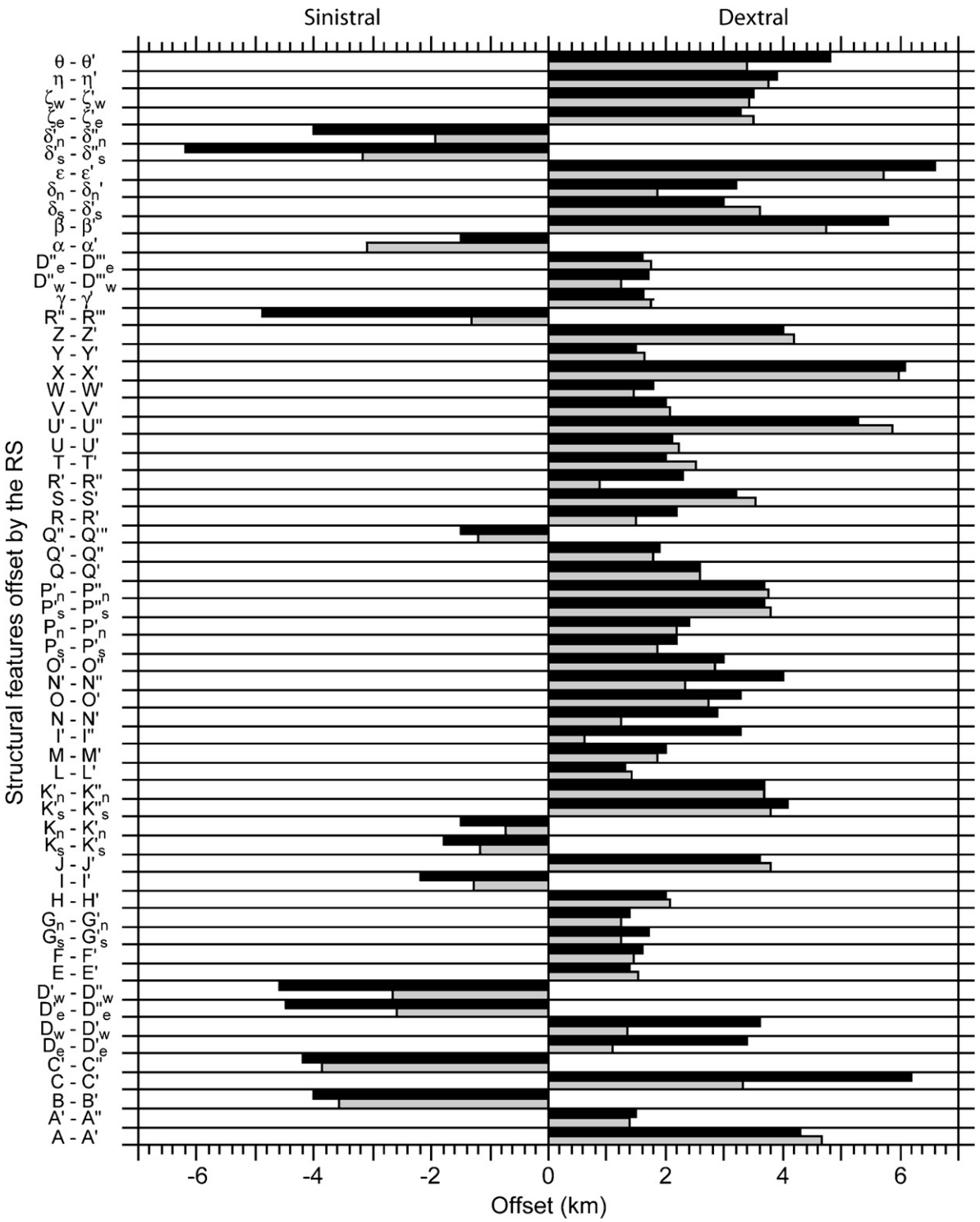

Fig. 6. Histogram of the measured (d_m – black bars) and calculated (d_c – gray bars) offsets of preexisting linear features along the RS. The RS is represented by the origin. Negative values correspond to sinistral offset and positive values to dextral offset.

coupled with the albedo and texture differences with the surrounding terrain, suggest it is also a band.

Examination of the preexisting terrain surrounding the western half of BLC_3 indicates the presence of at least 10 offset preexisting linear features along a ~100 km segment of the band (Fig. 8a). To get a first-order impression of the style of deformation responsible for the formation of this portion of the BLC, we performed a planar reconstruction of these offset preexisting features (Fig. 8c). The reconstruction indicates this band formed by some combination of extension and strike-slip motion.

Examination of BLC_3 indicates that the band can be subdivided into two swaths based on morphology and relative brightness (Fig. 8b and inset D). The southern swath of BLC_3, as seen in inset D, has a rougher texture and slightly

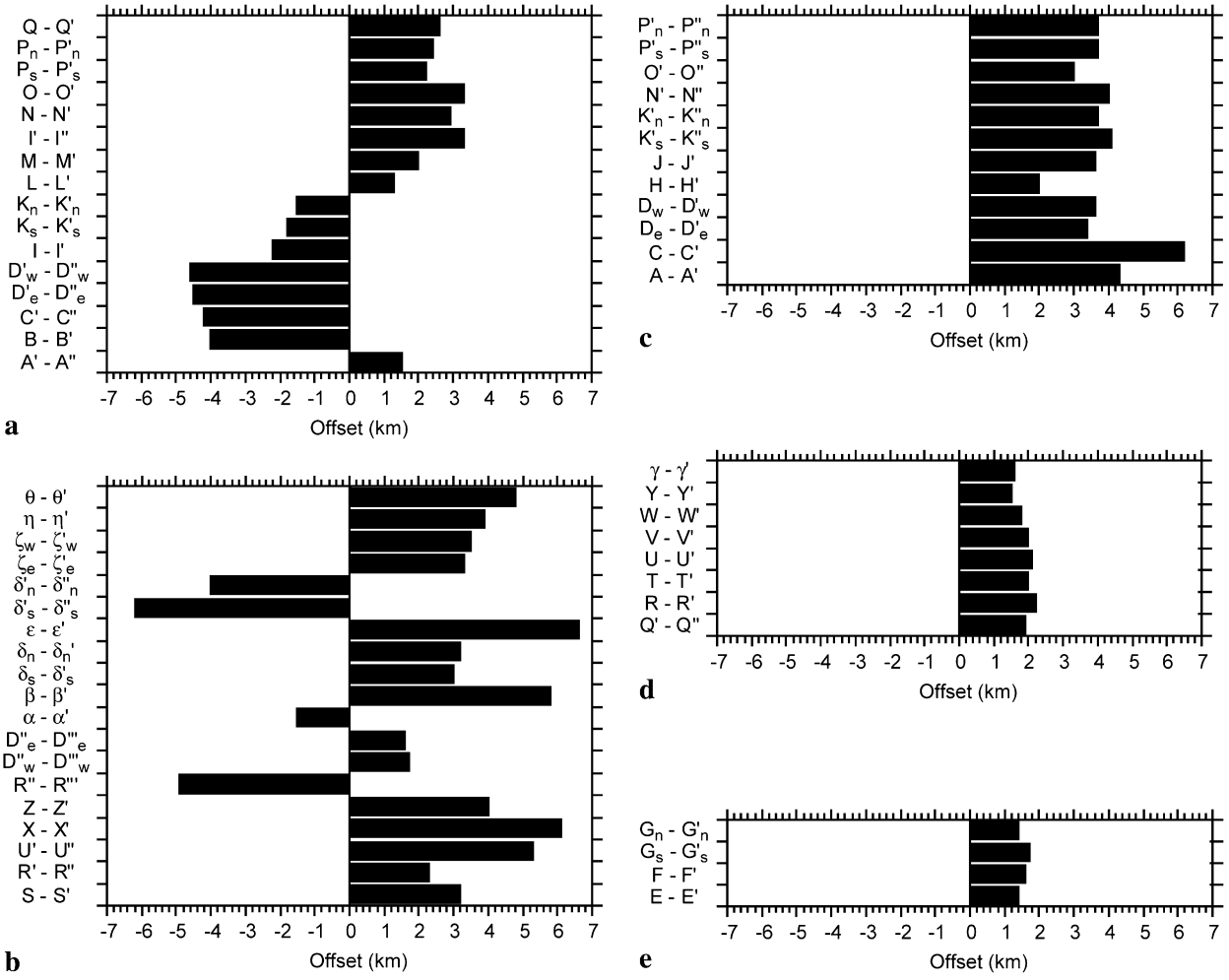

Fig. 7. Histograms of the offsets of preexisting linear features associated with various combinations of the events that formed the RS (represented by the origin). Negative values correspond to sinistral offset and positive values to dextral offset. (a) Preexisting linear features offset solely by RS_1. (b) Preexisting linear features offset by RS_1 and RS_2. (c) Preexisting linear features offset by RS_2 and RS_3. (d) Preexisting linear features offset solely by RS_3. (e) Preexisting linear features offset by RS_1, RS_2, and RS_3.

higher relative albedo than the northern swath. While the image resolution is insufficient to make a definitive interpretation of the meaning of these characteristics, we suggest they are reminiscent of some characteristics of Agenor Linea (Prockter et al., 2000). Agenor Linea may have formed as a result of dextral shear resulting in a series of strike-slip duplexes, perhaps combined with some extension, and an analogous interpretation may apply here.

The cross-cutting relationships between the BLC and the surrounding terrain are not as clear as for the RS. However, there is one E–W trending ridge that overlaps $BLC_{2\text{ and }3}$ (R of Fig. 8b). This ridge overlaps the RS as well, suggesting a similar upper limit on the relative age of the RS and BLC_3. Also, there are only three features (excluding the RS) that appear to overlap some portion of the BLC (Fig. 8b), suggesting a relatively young age for its formation.

2.3. Interactions between the RS and BLC

In the regional resolution coverage of the region surrounding Castalia Macula (Figs. 1 and 8), the RS terminates within the boundaries of the BLC at two locations: 9.7°S, 224.6°W and 9.3°S, 224.0°W. Both locations fall within the boundaries of what we have defined as BLC_3 (Fig. 8). One branch of the RS also intersects (and appears to terminate at) the BLC again ~550 km to the east at 1.9°S, 208.2°W (open circle on Fig. 1b). This relationship cannot be determined unambiguously, however, because of the lower resolution image coverage in that region. These relationships, along with the cross-cutting relationships of these two features with the surrounding terrain, suggest the RS and BLC were actively forming during the same period of time. This would then imply that these two features represent the margins of seven plates that were active in this region at that time (Fig. 1b).

2.4. Planar reconstructions of the region

Planar reconstructions of this region have been previously performed using the offsets of preexisting features as guides (Patterson and Pappalardo, 2002; Sarid et al., 2002). Patterson and Pappalardo (2002) presented a reconstruction involving

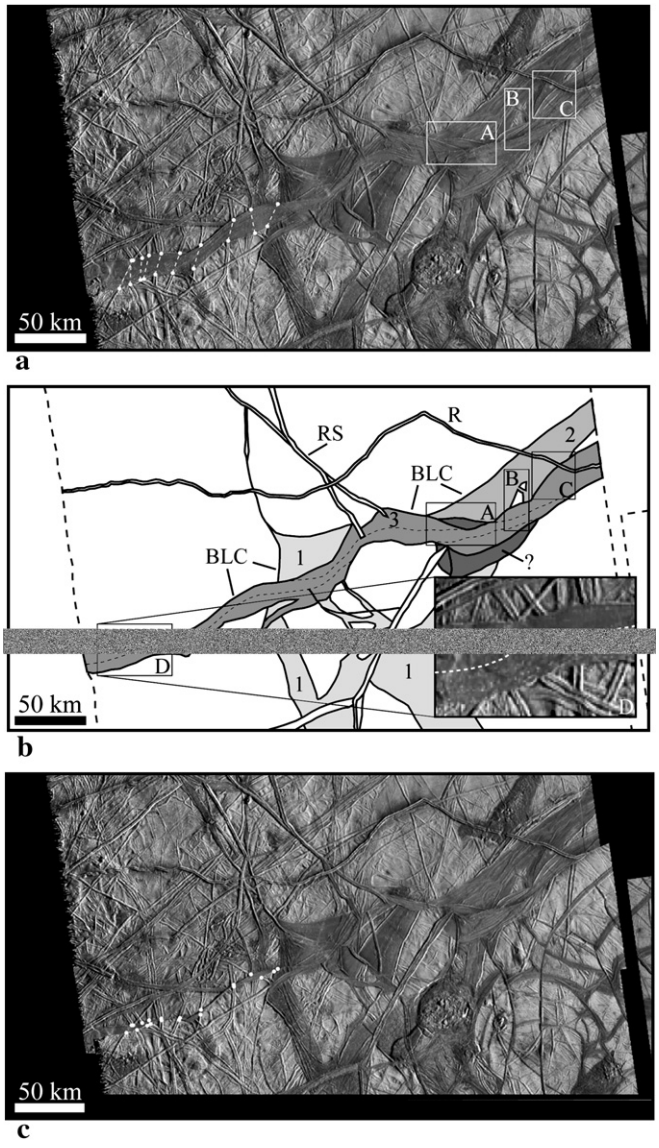

Fig. 8. (a) BLC, as imaged at 220 m/pixel. Locations of preexisting linear features offset by the BLC are indicated by paired white dots connected by dashed lines. Feature (A) shows a region where overlapping relationships are observed within the BLC. Feature (B) marks a region where preexisting terrain is observed within the boundaries of the BLC. In region (C), a bounding ridge extends within the boundaries of the BLC and overlaps portions of the interior of the BLC. (b) Sketch map of the inferred phases of formation of the BLC where 1–3 proceeds from oldest to youngest. Dashed lines within BLC_3 indicate a subdivision of the band based on morphology and relative brightness. Feature (D) illustrates differences in morphology and relative brightness within BLC_3 as discussed in the text. (c) A planar reconstruction of preexisting features identified in (a).

what we have defined as plates 2, 3, 4 and 6 (Fig. 1b), while Sarid et al. (2002) presented a reconstruction involving plates 3 and 4. Each reconstruction implicitly assumed that the plates involved behaved rigidly with respect to the surrounding terrain, and therefore all deformation associated with the reconstructions was accommodated at the boundaries of the plates.

The cross-cutting relationships of the RS with respect to the surrounding terrain, and the anomalous morphologic characteristics of the RS led Patterson and Pappalardo (2002) to suggest a planar reconstruction of the region involving transpression along the RS and BLC (Fig. 9a). Attempts by those authors to determine a finite pole of rotation for this reconstruction *a posteriori* using common terrestrially derived techniques (e.g., McKenzie and Parker, 1967; Gordon and Stein, 1992) were not successful. Patterson and Pappalardo (2002) suggested a mechanism for accommodating transpression along the RS, involving downward percolation of meltwater along a shear-heated ridge leading to surface collapse, following the model of Nimmo and Gaidos (2002). It was proposed that, over time, this process could accommodate surface contraction by the transport of material to the subsurface.

Sarid et al. (2002) also used the cross-cutting relationships of the RS with respect to the surrounding terrain, along with the morphology of the BLC, to suggest a reconstruction involving dextral strike-slip motion along the RS and convergence along the BLC. A reproduction of that reconstruction, based on the information provided in their manuscript, is shown in Fig. 9b. They stated that the morphology of the BLC was characteristic of sites of convergence. Specifically, they indicated that while the internal structure of the BLC could be considered analogous to bands on Europa, the margins of the feature were not parallel or reconstructable. The reconstruction of a similar feature (albeit on a much smaller scale) south of the BLC was also cited as indicating convergence. No mechanism to explain the loss of material along these features was provided.

Both previous reconstructions of this region left unresolved issues. In our reconstruction duplicating that of Sarid et al. (2002), there are three regions along the RS that overlap the surrounding terrain by several kilometers, post-reconstruction (Fig. 9b). Also, the offset magnitudes of the preexisting linear features E, F, and G of Fig. 2 increase significantly in this reconstruction. Finally, while both reconstructions indicated some degree of compression along the BLC, we find that BLC_3, which appears to have been actively forming in conjunction with the formation of the RS, is reconstructable via a combination of extension and strike-slip motion (Fig. 8c). It is not apparent that convergence has played any significant role in the formation of the BLC.

3. A method for determining finite rotations on Europa

Assuming that plates on a sphere move as rigid blocks, any displacement of a plate over a spherical surface from one position to another can be accomplished by a rotation, denoted by the quantity $\mathbf{R}[E,\Omega]$, of that plate by Ω degrees about a specific axis E (i.e., an Euler pole) passing through the center of the sphere. On Earth, this quantity can be determined using a number of techniques (e.g., Chase, 1978; Minster and Jordan, 1978; DeMets et al., 1990; Gordon, 1998). These commonly include using the trends of transform faults, the displacement azimuths of offset preexisting linear features along a plate boundary, and/or the matching of geomagnetic isochrons across plate boundaries involving oceanic crust.

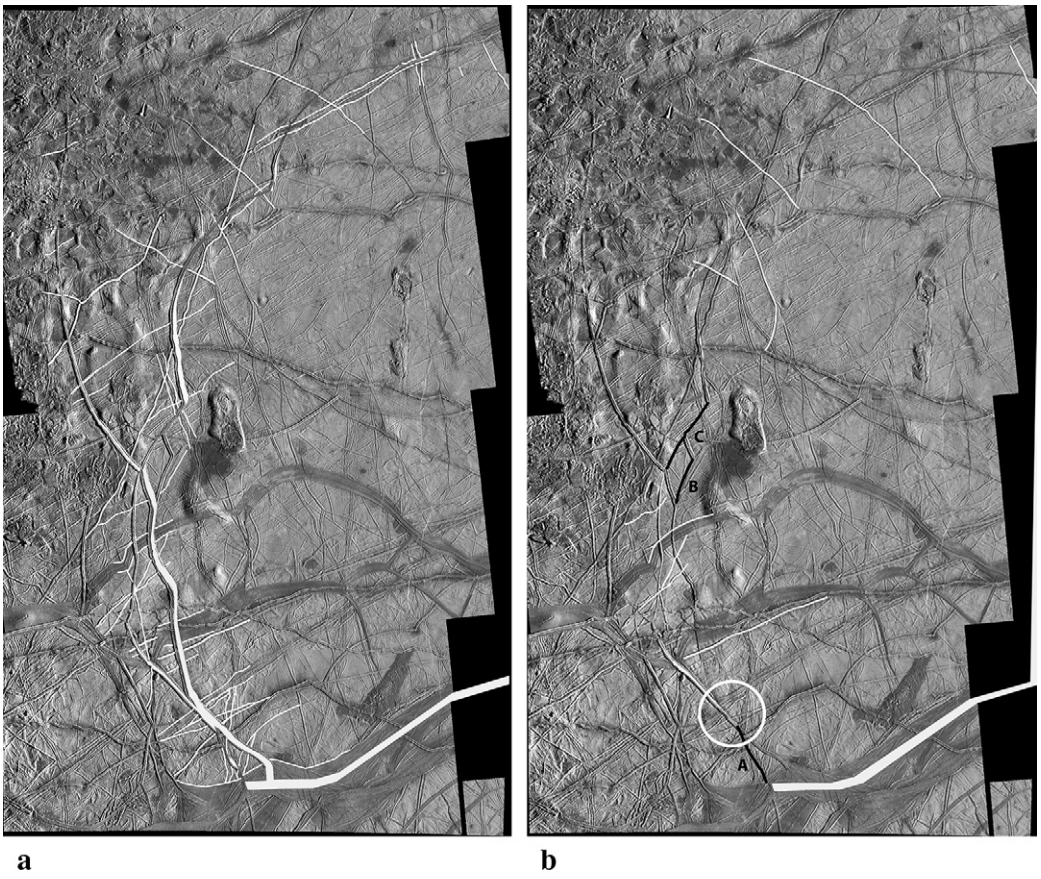

Fig. 9. (a) Planar reconstruction of plates 2, 3, 4 and 6 using the cross-cutting relationships of 60 offset preexisting features as a guide (white lines), following the approach of Patterson and Pappalardo (2002). White area represents material inferred to have been lost as a result of plate motion. (b) A reconstruction of plates 3 and 4 after Sarid et al. (2002), involving 10 preexisting offset linear features (white lines), using information provided in their manuscript. Black lines labeled A–C indicate regions where we find significant overlap of preexisting terrain, and white circle indicates region where offsets of preexisting features have increased significantly as a result of the reconstruction. White area represents material inferred to have been lost as a result of plate motion.

More recently, space geodesy has also been employed (e.g., Gordon and Stein, 1992; Kogan et al., 2000; Sella et al., 2002).

On Europa, strike-slip features are ubiquitous and there is abundant evidence for offset features, permitting at least two means of determining the relative motions between rotated plates. Schenk and McKinnon (1989) used the trend of transform-like strike-slip faults they identified as associated with the formation of extensional features on Europa's anti-Jovian hemisphere to determine an Euler pole for the opening of those features. Pappalardo and Sullivan (1996) used the displacement azimuths of preexisting features along Thynia Linea to determine a best-fit pole of opening for that extensional feature.

The modeling technique we have developed determines a finite pole of rotation, $\mathbf{R}[E,\Omega]$, for the reconstruction of a two-plate system using the trends and offsets of preexisting features along a plate boundary as inputs. This method employs an iterative grid-search technique that allows testing of all combinations of finite pole location E and rotation Ω within a given grid size and spacing. The result is a map of the rotation Ω for each possible Euler pole E that yields a least-squares minimum for the offsets of all the features used as inputs. The location on this map with the minimum value then represents the best-fit $\mathbf{R}[E,\Omega]$ for that two-plate system. This method is also applicable to multi-plate systems provided they can be confidently divided into a collection of two-plate systems.

3.1. Defining a pole of rotation

The proceeding description of poles of rotation follows Moores and Twiss (1995). In Cartesian coordinates, a rotation R_{jk} is described by the relationship between a reference set of three mutually orthogonal axes and a second set that has been rotated relative to the reference axes. The rotation is defined by the cosines of the angles between each rotated axis θ_{jk} and each of the three reference axes,

$$R_{jk} = \cos\theta_{jk} \tag{1}$$

where θ_{jk} is the angle between the jth coordinate of the reference frame and the kth coordinate of the rotated frame. These cosines are arranged in a 3×3 rotation matrix:

$$R = \begin{bmatrix} R_{11} & R_{12} & R_{13} \\ R_{21} & R_{22} & R_{23} \\ R_{31} & R_{32} & R_{33} \end{bmatrix} \tag{2}$$

denoted by R_{jk} (for j and $k = 1, 2, 3$). This matrix may be determined from the Cartesian components of the Euler pole $E = [E_1, E_2, E_3]$ and the rotation magnitude Ω, giving:

$$\begin{bmatrix} R_{11} \\ R_{21} \\ R_{31} \end{bmatrix} = \begin{bmatrix} E_1E_1(1-\cos\Omega)+\cos\Omega \\ E_2E_1(1-\cos\Omega)-E_3\sin\Omega \\ E_3E_1(1-\cos\Omega)+E_2\sin\Omega \end{bmatrix}$$
$$\begin{bmatrix} R_{12} \\ R_{22} \\ R_{32} \end{bmatrix} = \begin{bmatrix} E_1E_2(1-\cos\Omega)+E_3\sin\Omega \\ E_2E_2(1-\cos\Omega)+\cos\Omega \\ E_3E_2(1-\cos\Omega)-E_1\sin\Omega \end{bmatrix} \quad (3)$$
$$\begin{bmatrix} R_{13} \\ R_{23} \\ R_{33} \end{bmatrix} = \begin{bmatrix} E_1E_3(1-\cos\Omega)-E_2\sin\Omega \\ E_2E_3(1-\cos\Omega)+E_1\sin\Omega \\ E_3E_3(1-\cos\Omega)+\cos\Omega \end{bmatrix}$$

With only three independent variables (latitude, longitude, and angle of rotation), a finite pole of rotation can often be represented as a vector quantity. However, when adding finite rotations it is important to remember that rotation poles are matrices, and that matrix addition is not commutative.

3.2. Determining a best-fit rotation

For each preexisting offset linear feature along a given plate margin, the locations of three points are determined: A_i , B_i , and C_i (Table 1). As illustrated in Fig. 10, points A_i and B_i are located along a preexisting offset linear feature on a fixed plate, and C_i is located on the corresponding offset linear feature on the plate to be rotated. Using A_i and B_i, we can determine a plane that passes through the center of the sphere and represent that plane by its vector normal N_i:

$$\begin{aligned} N_x &= \left(A_yB_z - A_zB_y\right)/\sin\delta \\ N_y &= \left(A_zB_x - A_xB_z\right)/\sin\delta \\ N_z &= \left(A_xB_y - A_yB_x\right)/\sin\delta \\ \delta &= \cos^{-1}\left(A_xB_x + A_yB_y + A_zB_z\right) \end{aligned} \quad (4)$$

Given the normal, we can then calculate the distance,

$$d_c = |\overrightarrow{AC}_x N_x + \overrightarrow{AC}_y N_y + \overrightarrow{AC}_z N_z| \quad (5)$$

from the third point C_i to this plane. The distance, d_c, represents a measure of the offset of this preexisting linear feature across the plate margin that we want to reconstruct (Table 1 and Fig. 6). It is the perpendicular distance from C_i to the plane and, therefore, will differ from the measured offset d_m in Table 1 and Fig. 6 when the strike of the RS is not perpendicular to the offset being measured. The magnitude of this difference is dependent on the geometry of the intersection of a given preexisting offset linear feature and the RS (Fig. 10).

Differences between the measured and calculated offset are not important to the results of our modeling technique. Our goal is to determine a rotation that minimizes the offsets of all preexisting linear features input regardless of the method in which the offsets are measured. Our reason for using d_c is a matter of mathematical convenience. Using this method of measuring offset, we can iteratively apply a number of possible rotation matrices to C_i:

$$\begin{bmatrix} C_x \\ C_y \\ C_z \end{bmatrix} \begin{bmatrix} R_{11} & R_{12} & R_{13} \\ R_{21} & R_{22} & R_{23} \\ R_{31} & R_{32} & R_{33} \end{bmatrix} = \begin{bmatrix} C_{x'} \\ C_{y'} \\ C_{z'} \end{bmatrix} \quad (6)$$

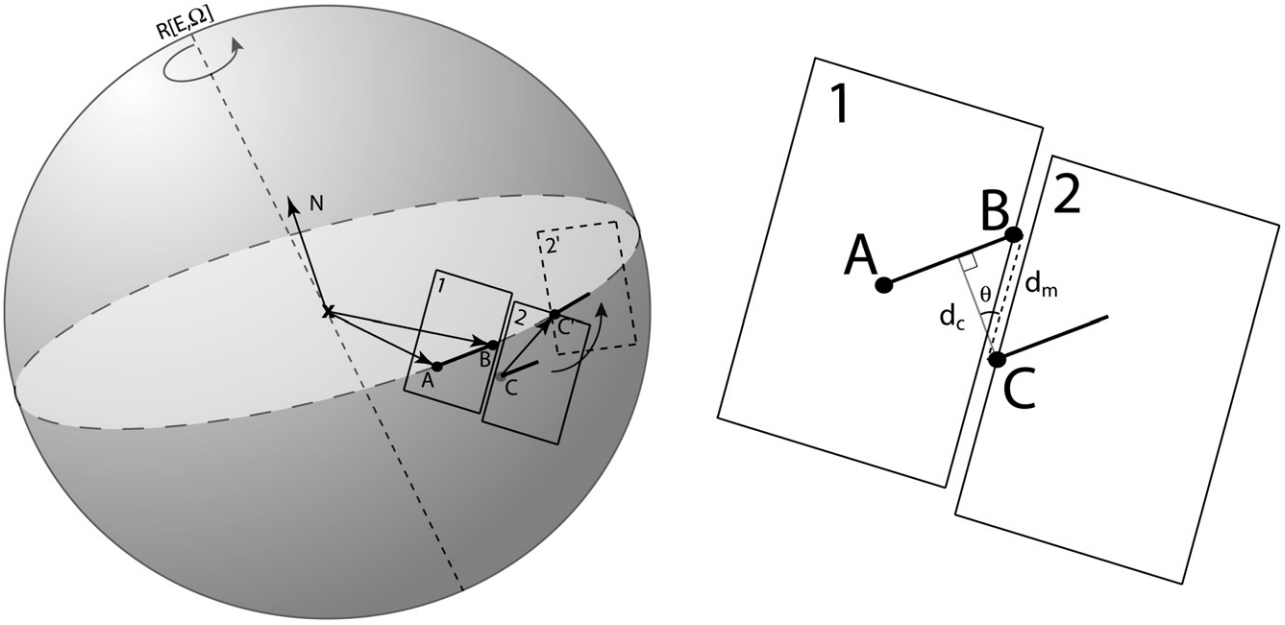

Fig. 10. Illustration of inverse modeling technique. The sphere represents Europa. A and B represent points on an offset linear feature lying on a fixed plate (box 1), and C represents a point on the same offset linear feature lying on the plate to be rotated (box 2). N is the vector normal to the plane represented by the points A and B. The measured offset, d_m (dashed line), between points B and C and the calculated offset, d_c (gray line) between the plane AB and the point C are shown. They are separated by the angle θ. C′represents the position of the offset feature and plate (dashed box 2′) after rotation about the finite pole of rotation $\mathbf{R}[E,\Omega]$.

and use Eq. (5) after each rotation to determine the distance from C_i' to N_i. The rotation matrix **R** that produces the least-squares minimum distance from C_i' to N_i then represents the best-fit pole of rotation for the reconstruction of the preexisting linear features across this plate margin (Fig. 10). The uniqueness of the pole of rotation found using this method is determined with confidence regions X at the 95 and 99% level. We use an F-test:

$$X = X_{\min}(1 + (N/M - N)F[N, M - N, 1 - \alpha])^{1/2} \quad (7)$$

to determine these confidence regions, where $X_{\min}$ refers to the least-squares minimum value determined for the best-fit reconstruction used, M and N represent the number of data points and degrees of freedom, respectively, and $F[\ ]$ refers to an F-table with the axes N and $M-N$ at the $1-\alpha$ confidence level (Draper and Smith, 1981). A finite pole of rotation has 3 degrees of freedom. This imposes a requirement of at least four inputs (i.e., four offset linear features) into our model to produce confidence regions.

3.3. Sources of error

There are two possible sources of systematic error in the general application of this modeling technique. The first results from how the locations of A_i–C_i are determined. These points are determined manually by inspection of images associated with the region to be reconstructed. Errors in these locations from feature to feature can occur on the pixel-scale. The effects of this source of error increase as the resolution of the images used approaches $|B_i - C_i|$.

The second source of error results from the grid resolution used in our modeling technique. To ensure all possible locations for a finite pole of rotation are represented in the model, a hemispherical location E grid is used (0–90° latitude and 0–360° longitude) and the resolution is set to 1° increments. Because of the computational demands of our modeling technique, it is not possible to increase the increments with which we test locations to better than $1^\circ \times 1^\circ$ ($\sim 27 \times 27$ km at Europa's equator) without dramatically reducing the latitude and longitude range of the locations tested. Therefore, we vary the increments with which Ω is tested from 10s of degrees in 1° increments to 2° in 0.01° increments in order to best determine E for each set of inputs.

4. Results

Following McKenzie and Parker (1967), when describing plate rotations in this analysis we have used the convention ${}_A\mathbf{E}_B$, where **E** represents the pole of rotation (as opposed to **R** in the previous section), the left subscript indicates the plate on which the reference coordinates are fixed, and the right subscript indicates the plate whose rotation or motion is described from those coordinates. In other words, ${}_A\mathbf{E}_B$ indicates the pole of rotation for the reconstruction of plate B with respect to plate A.

We use the initial variance V_i:

$$V_i = \sqrt{\frac{\sum x_j^2}{N}} \quad (8)$$

when describing the pre-reconstruction offsets of all preexisting features along the boundary between the two plates we are attempting to reconstruct. We use the final variance V_f:

$$V_f = \sqrt{\frac{\sum x_j^2}{N - M}} \quad (9)$$

when describing the post-reconstruction residual offsets. In these equations x_j represents the offset of a given feature, N represents the total number of offset features, and M represents the number of degrees of freedom.

4.1. Reconstructing plates defined by the RS and BLC using finite poles of rotation

Within the multi-plate system defined by the RS and BLC (Fig. 1b), we are primarily concerned with determining ${}_1\mathbf{E}_4$. We choose these two plates because their margins consist of both the RS and BLC, and all phases of the formation of the RS are recorded along some portion of their margins. The decision to leave plate 1 fixed and rotate plate 4 is based on the available image data (i.e., the margins of plate 4 are fully imaged). To determine ${}_1\mathbf{E}_4$ with our modeling technique, we have elected to take two complimentary approaches.

The first approach assumes that the seven-plate system defined by the RS and BLC (Fig. 1b) can be approximated as a two-plate system. We use ${}_{1*}\mathbf{E}_4$ to describe this finite pole of rotation. The justification for this assumption relies on the spatial and temporal relationships of the RS and BLC with respect to each other and with respect to the surrounding terrain (as discussed in Section 2). By making this assumption we can supply a greater number of inputs to our modeling technique and thus better constrain the determination of a finite pole of rotation. This assumption was also implicitly used in the planar reconstructions suggested by Patterson and Pappalardo (2002) and Sarid et al. (2002) and represents the simplest means of reconstructing this multi-plate system.

In the second approach, the region is divided into five two-plate systems. From these five systems, we are able to provide three determinations of ${}_1\mathbf{E}_4$: one by using a shared plate margin between plates 1 and 4 (Fig. 5d), and two others by the additions of the finite rotations ${}_1\mathbf{E}_2 + {}_2\mathbf{E}_4$ and ${}_1\mathbf{E}_3 + {}_3\mathbf{E}_4$. These determinations use fewer observational inputs and, as a result, may not be as well constrained. However, they do allow us to test the approximation used in the first approach and also the assumption that the plates involved behaved rigidly while they deformed.

4.1.1. Determining ${}_{1*}\mathbf{E}_4$

As discussed in Section 2.1, the cross-cutting relationships of the ridges that comprise the RS suggest they are related

spatially and temporally. It is possible, based on these relationships that RS_{1-3} occurred relatively rapidly and, therefore, that all phases of the formation of the RS could be approximated as the result of a single deformation event. If so, the offsets of preexisting linear features for all of the ridges associated with the RS should be reconstructable about the same finite rotation pole. This approximation allows us to determine a finite pole of rotation for plate 4 with respect to the six other plates identified in Fig. 1b, thereby reducing this complex multi-plate system to a simple two-plate system. For convenience, we designate this combined fixed plate as 1* (Fig. 11).

For the application of our modeling technique to this scenario, we use 27 preexisting offset linear features along the boundary between plates 4 and 1* as inputs (Table 2). We find that a reconstruction can be performed that decreases the variance of these offsets by an order of magnitude if plate 4 is rotated by -0.43° (negative defined as clockwise) about an Euler pole at 11 °N, 253 °W. Fig. 12a shows the location of this best-fit finite pole of rotation, with 95 and 99% confidence regions, on the hemispherical grid map used with our modeling technique. For this finite pole of rotation, a comparison of the pre- and post-reconstruction calculated offsets d_c of preexisting linear features along the RS is shown in Fig. 13. The figure indicates that a reconstruction using the best-fit pole determined does result in a general reduction in offset magnitude for the preexisting linear features used as inputs. However, it also appears that the reduction in offset magnitude is nonsystematic. This is an indicator that the two-plate approximation made in this approach the notation may not be appropriate and/or that one or more of the plates involved may have behaved nonrigidly.

Provided the assumptions made regarding plates 1* and 4 are appropriate, an image-based representation of the reconstruction of these plates about ${}_{1*}\mathbf{E}_4$ (Fig. 11) suggests that $\sim 1900\ km^2$ of the surface of Europa would have been lost during the deformation event that created the BLC and RS (gray region of Fig. 11). The majority of this material seems to have been lost along the southern extent of the RS. This reconstruction implies a loss of $\sim 1\%$ of the surface area of the plate 4 ($1.6 \times 10^5\ km^2$) along a convergent boundary comprised by the RS. Mechanisms that could be responsible for the loss of surface material along ridges include: (1) melting and subsidence along ridges induced by shear heating (Patterson and Pappalardo, 2002; Nimmo and Gaidos, 2002); and (2) compression due to loss of porosity (Aydin, in this issue).

This reconstruction implies that the BLC was modified primarily by left-lateral strike-slip motion during the formation of the RS (Fig. 11). This result is consistent with our interpretation that strike-slip motion was involved in the formation of BLC_3. This is not consistent with either of the previous planar reconstructions of this region (Patterson and Pappalardo, 2002; Sarid et al., 2002). However, the interpretation that the RS accommodated surface contraction is shared with the planar reconstruction of Patterson and Pappalardo (2002).

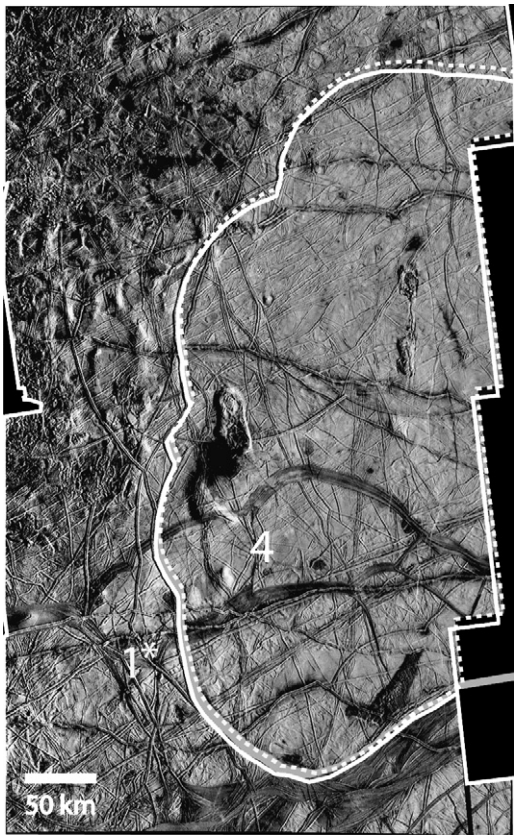

Fig. 11. Reconstruction of Castalia Macula region (E17REGMAP01 mosaic centered at ~0° lat. and 227° lon.) using an Euler pole at 11 °lat., 253 °lon. and a rotation of −0.43 °. This reconstruction assumes the region can be approximated as a two-plate system, where plate 1* represents plates 1–3 and 5–7 in Fig. 1b. Image resolution is 220 m/pixel. Solid white line indicates position of the plate before reconstruction and dashed white line indicates position after. Gray region between plates 1* and 4 indicates material that would have been lost as a result of the rotation of plate 4 with respect to plate 1*.

4.1.2. Determining ${}_1\mathbf{E}_4$

Using the cross-cutting relationships among the ridges that comprise the RS (Fig. 4), it is also possible to reconstruct plate 4 without reducing RS_{1-3} to a single event. This requires any

Table 2

Finite rotation	Model inputs	Location (°)		Rotation (°)	V_i (km^2)	V_f (km^2)
		Lat.	Lon.			
${}_{1*}\mathbf{E}_4$	B, C′, E, F, Gs, H, J, K′s, K′n, N′, O′, P′s, P′n, S, R′, U′, X, Z, R″, α, β, δs, ε, δ′s, ζe, η, θ	11	253	−0.43	13.00	1.67
${}_1\mathbf{E}_4$	E, F, Gs, Gn	9	47	1.9	1.92	0.0363
${}_1\mathbf{E}_2$	R, T, U, V, W, Y, γ	8	217	0.32	3.70	0.0904
${}_2\mathbf{E}_4$	S, R′, U′, X, Z, R″, α, β, δs, δn,ε, δ′s, δ′n, ζe, ζw, η, θ	0	28	−0.67	14.54	0.691
${}_1\mathbf{E}_3$	L, M, I′, N, O, Ps, Pn, Q	5	53	0.93	3.49	0.236
${}_3\mathbf{E}_4$	H, J, K′s, K′n, N′, O′, P′s, P′n	4	49	4.31	11.12	0.331
${}_1\mathbf{E}_3 + {}_3\mathbf{E}_4$	–	4.2	50	5.2	–	–
${}_1\mathbf{E}_2 + {}_2\mathbf{E}_4$	–	2.6	211	0.99	–	–

${}_1\mathbf{E}_3 + {}_3\mathbf{E}_4$ and ${}_1\mathbf{E}_2 + {}_2\mathbf{E}_4$ do not have model inputs or values for the variance as they were not determined using the modeling technique.

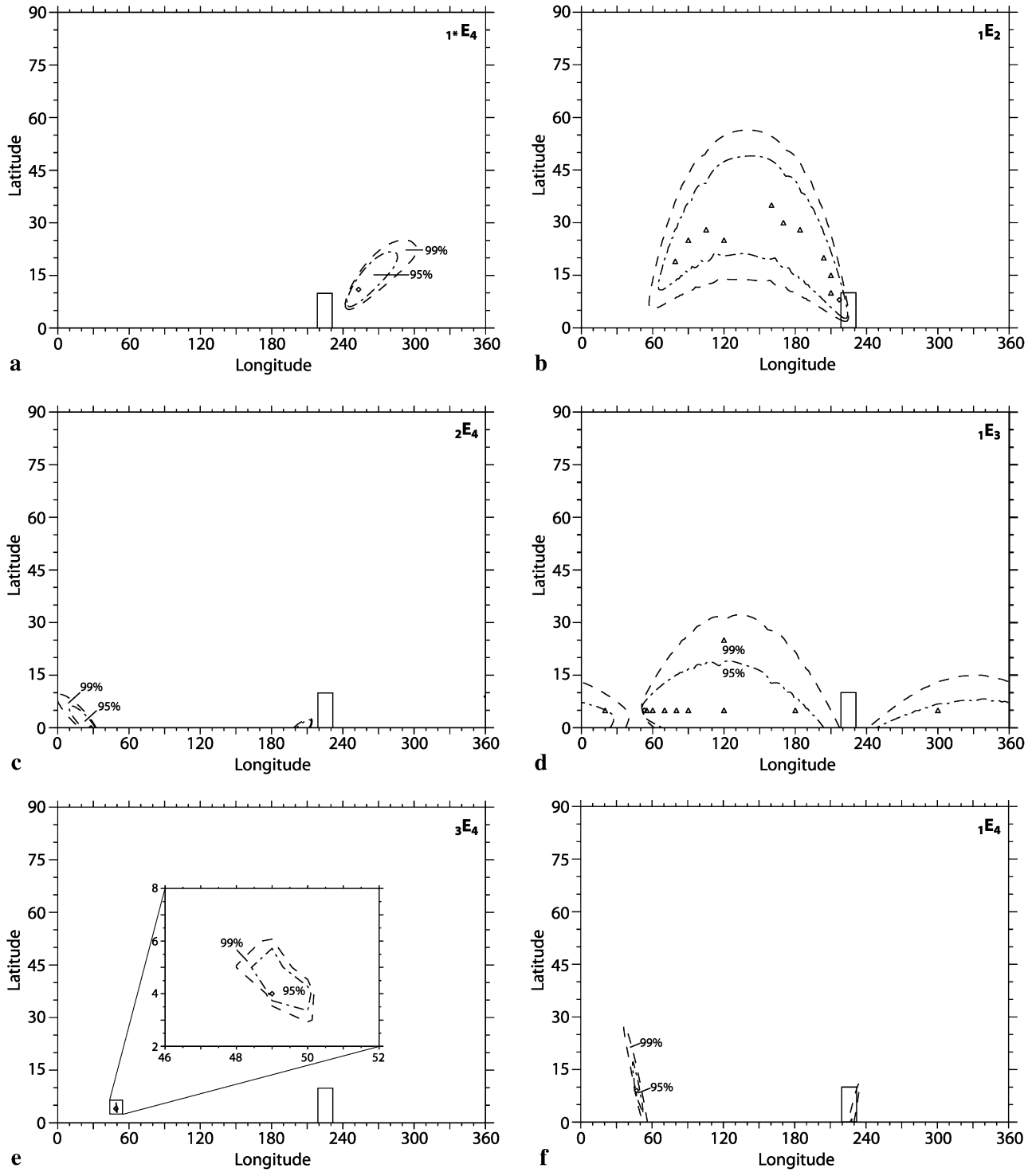

Fig. 12. Locations of finite poles of rotation (a) with the simplifying assumption of a two-plate system and (b–f) finite poles of rotation for set of five two-plate systems in the region. Curves indicate 99% (dashed) and 95% (dot-dashed) confidence regions. Only the northern hemisphere poles are shown. Box on each plot represents that location of the study region. Triangles (a and c) indicate locations of alternative finite rotation poles used in our error analysis (see text).

of the deformation events that affected some portion of the boundary of this plate be accounted for in a reconstruction. Based on Fig. 5d, it is apparent that portions of the boundary of plate 4 (Fig. 1b) were forming or being modified during RS_{1-3}. Therefore, a reconstruction for plate 4 can only be determined if a portion of the boundary of the plate was active during RS_{1-3} and/or if a combination of rotations can be found that reconstructs the effects of RS_{1-3} on plate 4.

Using Fig. 5d as a guide, the RS can be divided into five "regions," each having been active during a different

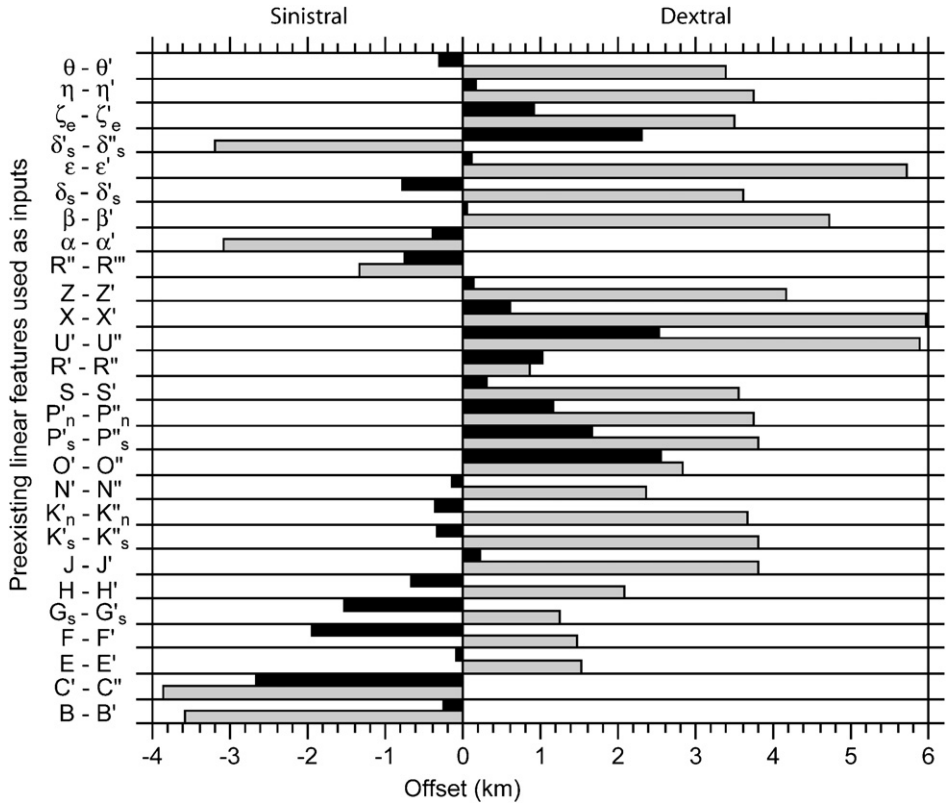

Fig. 13. Histogram of the pre-reconstruction (black bars) and post-reconstruction (gray bars) calculated offsets of preexisting linear features along the RS (represented by the origin) using the finite pole of rotation ${}_{1*}\mathbf{E}_4$. Negative values correspond to sinistral offset and positive values to dextral offset.

combination of events RS_1, RS_2, and/or RS_3. These regions act as plate boundaries and, therefore, effectively form five two-plate systems. The boundary between plates 1 and 4 is one of these regions and was active during RS_{1-3}. This suggests the finite rotation ${}_1\mathbf{E}_4$ (Table 2 and Fig. 12f) can be used to reconstruct plate 4 with respect to all deformation events that were involved in the formation of the RS. The finite rotation ${}_1\mathbf{E}_4$ can also be determined using this set of five two-plate systems by the additions of the finite rotations ${}_1\mathbf{E}_2 + {}_2\mathbf{E}_4$ and ${}_1\mathbf{E}_3 + {}_3\mathbf{E}_4$. Best-fit finite poles of rotation for these five two-plate systems are given in Table 2 and shown, with confidence regions, in Fig. 12b–e.

For ${}_1\mathbf{E}_4$ using the common boundary between plates 1 and 4, we find that the variance of the preexisting offset linear features along this boundary can be reduced by two orders of magnitude if plate 4 is rotated with respect to plate 1 by 1.9° about an Euler pole located at 9° lat. and 47° lon. This determination of ${}_1\mathbf{E}_4$ differs significantly from the determination of ${}_{1*}\mathbf{E}_4$, and the confidence regions of the two finite poles of rotation do not overlap (Fig. 12a and f). Similar to the results of Fig. 13 in the previous section, this suggests that the two-plate approximation used in the first approach was not appropriate and/or that one or more of the plates involved in this analysis did not behave rigidly. To determine which of these possibilities better accounts for nonsystematic reduction in offset magnitude for ${}_{1*}\mathbf{E}_4$ and the discrepancy between ${}_1\mathbf{E}_4$ and ${}_{1*}\mathbf{E}_4$, we next consider the determinations of ${}_1\mathbf{E}_4$ by the additions of ${}_1\mathbf{E}_2 + {}_2\mathbf{E}_4$ and ${}_1\mathbf{E}_3 + {}_3\mathbf{E}_4$.

The addition of finite rotations is a straightforward process involving the matrix multiplication of the poles of rotation involved. However, the poles of rotation must be combined in the order they occurred, since matrix multiplication is not commutative. To determine the order in which plate rotations are combined for this region, we use the cross-cutting relationships shown in Fig. 4. The addition of the finite poles of rotation ${}_1\mathbf{E}_2$ and ${}_2\mathbf{E}_4$ suggests that ${}_1\mathbf{E}_4$ is located at 2.6°N, 211°W with a rotation of 0.99° (Table 2). The addition of ${}_1\mathbf{E}_3$ and ${}_3\mathbf{E}_4$ suggests that ${}_1\mathbf{E}_4$ is located at 4.2°N, 50°W with a rotation of 5.2°. Both of these determinations of ${}_1\mathbf{E}_4$ differ significantly from each other and from the previous determination of ${}_1\mathbf{E}_4$. They also both differ from ${}_{1*}\mathbf{E}_4$.

We have already suggested that, for our first approach to have been valid, ${}_{1*}\mathbf{E}_4$ and ${}_1\mathbf{E}_4$ should be equivalent, or at least fall within the confidence regions of one another. If the discrepancy is a result of the two-plate approximation made in the first approach, then our determination of ${}_1\mathbf{E}_4$ by the additions of ${}_1\mathbf{E}_2 + {}_2\mathbf{E}_4$ and ${}_1\mathbf{E}_3 + {}_3\mathbf{E}_4$ would differ from ${}_{1*}\mathbf{E}_4$ but be equivalent to the first determination of ${}_1\mathbf{E}_4$. Since none of the determinations of ${}_1\mathbf{E}_4$ are equivalent to each other or to ${}_{1*}\mathbf{E}_4$ (Table 2), we are led to the conclusion that one or more of the plates involved in the multi-plate system defined by the RS and BLC behaved nonrigidly.

4.2. Quantifying nonrigid behavior

We approximate the degree to which this system deviates from rigid behavior by calculating a difference rotation ($_1\mathbf{D}_4$) between any two of the three determined values of $_1\mathbf{E}_4$. This is accomplished by multiplying one determination of $_1\mathbf{E}_4$ by the inverse of another determination, specifically:

$$_1\mathbf{D}_4^a = (_1\mathbf{E}_2 + {}_2\mathbf{E}_4)(_1\mathbf{E}_3 + {}_3\mathbf{E}_4)^{-1} \quad (10a)$$

or

$$_1\mathbf{D}_4^b = (_1\mathbf{E}_2 + {}_2\mathbf{E}_4)^{-1}(_1\mathbf{E}_3 + {}_3\mathbf{E}_4) \quad (10b)$$

where a and b are antipodes of the difference pole of rotation **D**. An arbitrary boundary is then placed between the plates that comprise these two determinations of $_1\mathbf{E}_4$, and a point on that boundary is rotated about the difference pole. The distance between the original location of that point and its location after rotation about the difference pole provides an indication of the amount of deformation that has been distributed within one or more of the plates involved.

Using this method, a difference rotation between the determinations of $_1\mathbf{E}_4$ by the matrix additions of $_1\mathbf{E}_2 + {}_2\mathbf{E}_4$ and $_1\mathbf{E}_3 + {}_3\mathbf{E}_4$ is found at 3°S, 226.8°W with −6.2° of rotation for $_1\mathbf{D}_4^a$, and at 3.3°N, 46.7°W with 6.2° of rotation for $_1\mathbf{D}_4^b$ (Table 3). These values are approximately antipodal, as expected. An arbitrary boundary was then placed between these sets of plates at 1.85°N extending east and west across the image and a point was placed on that boundary at 227.5°W (Fig. 2). By applying the rotation $_1\mathbf{D}_4^a$ to this point, it is rotated 1.98 km to the northeast. The application of $_1\mathbf{D}_4^b$, results in a rotation of 2.31 km to the northeast. These two results indicate that kilometers of deformation associated with the rotation of plates 2, 3, and/or 4 with respect to plate 1 was accommodated internally rather than along the plate margins.

4.3. Error analysis

As discussed in Section 3.3, systematic errors associated with the general application of this modeling technique include determining the locations of A_i–C_i and the grid resolution of the model. To minimize the effects of the former, we used the higher resolution portion of the available image coverage (Fig. 1a) to determine the locations A_i–C_i. The pixel dimensions in that region (~220 m/pixel) are an order of magnitude less than the average offsets of the features used to determine poles of rotation (~1–7 km, Table 1). Also, for consistency, the locations of A_i–C_i were chosen to be the axial troughs of double ridges or the boundaries of bands and complex ridges for each offset feature used as a model input. For the latter, we used lower resolution rotation grids to test the stability of the determined finite poles.

Another source of error that was not discussed in the general application of this modeling technique, but could affect the conclusions drawn from this analysis, deals with the confidence regions of the finite poles of rotation we have determined. We use both $_1\mathbf{E}_2$ and $_1\mathbf{E}_3$ to determine a finite rotation for $_1\mathbf{E}_4$ and the difference rotations $_1\mathbf{D}_4^a$ and $_1\mathbf{D}_4^b$, and each of these poles of rotation have confidence regions that cover a significant portion of the globe (Fig. 12b and d). This indicates that a large number of finite rotations would produce essentially equivalent reconstructions of the features involved. This raises the question: would other finite rotation poles within the confidence regions cause significant variations in our results?

To answer this question, we have performed the same difference rotation calculation on 10 additional finite rotations which fall within the confidence regions of our determinations of $_1\mathbf{E}_2$ and $_1\mathbf{E}_3$ (triangles in Fig. 12b and d). The results are presented in Table 3. Additional values of the finite rotation $_1\mathbf{E}_2$ were used to determine $_1\mathbf{D}_4^a$ and resulted in a mean value for the amount of deformation distributed within one or more of the plates of 2.14+/−0.14 km. For this calculation then, 6 of 10 values for $_1\mathbf{D}_4^a$ fall within 1 standard deviation of the mean and all values fall within 2 standard deviations (Table 3). Additional values for $_1\mathbf{E}_3$ were used to determine $_1\mathbf{D}_4^b$ and resulted in an average value of 2.22+/−0.27 km. Similarly for this calculation, 8 of 10 values fall within 1 standard deviation of the mean and all values fall within 2 standard deviations. Our general conclusion from these results is that alternative poles of rotation within the confidence regions of $_1\mathbf{E}_2$ and $_1\mathbf{E}_3$ do not affect our analysis.

Table 3

Pole location (°)			Difference pole location (°)			Distance (km)
Lat.	Lon.	Rot.	Lat.	Lon.	Rot.	
$_1\mathbf{E}_2$						
8	**217**	**0.32**	**−3.0**	**226.8**	**−6.2**	**1.98**
10	210	0.22	−3.1	226.7	−6.1	2.22
15	210	0.19	−3.0	226.8	−6.0	1.93
28	184	0.10	−3.1	226.7	−5.9	2.10
20	204	0.15	−3.1	226.8	−6.0	1.95
35	160	0.08	−3.2	226.7	−5.9	2.10
30	170	0.09	−3.2	226.7	−5.9	2.24
28	105	0.09	−3.2	226.7	−5.8	2.30
25	90	0.10	−3.2	226.7	−5.8	2.14
19	79	0.13	−3.3	226.7	−5.8	2.23
25	120	0.08	−3.3	226.6	−5.8	2.37
$_1\mathbf{E}_3$						
5	**53**	**0.93**	**3.3**	**46.7**	**6.2**	**2.31**
5	55	0.70	3.2	46.7	5.9	2.22
5	60	0.43	3.1	46.7	5.7	2.15
5	70	0.24	3.1	46.6	5.5	2.16
5	80	0.17	3.0	46.6	5.5	2.21
5	90	0.14	3.0	46.6	5.4	2.10
5	120	0.09	3.0	46.5	5.3	2.31
5	180	0.11	3.1	46.5	5.2	2.46
5	300	−0.10	2.9	46.8	5.3	1.75
5	20	−0.20	2.9	46.6	5.1	1.97
25	120	0.08	3.3	46.4	5.3	2.82

Bold indicates values determined using the best fit poles for each two-plate system.

5. Implications

5.1. Tectonic history of the Castalia Macula region during the formation of the RS and BLC

Examination of the morphology and cross-cutting relationships of the RS indicate that it represents a single throughgoing structure that comprised a collection of ridges that are relatively young and formed in three distinct phases. The length of time required to form the RS is uncertain but cross-cutting relationships with respect to the surrounding terrain suggest the RS, and hence the events that formed it, are related. The offsets of the majority of preexisting features along the RS indicate formation by some component of dextral shear (Fig. 6 and Table 1). However, nonsystematic variations in the offset magnitude of these features, coupled with evidence for sinistral offsets of some preexisting features, suggest a more complex deformation history. Two possible explanations for this added complexity are a component of compression along portions of the RS during its formation and/or the presence of nonrigid plate behavior.

It has been suggested previously that the morphology of the BLC may be characteristic of plate convergence on Europa (Sarid et al., 2002). However, we find no evidence in the morphology or cross-cutting relationships of this feature to suggest that it is a convergent boundary. Instead, our examination of the feature indicates it represents a collection of relatively young superposed bands with morphologies that have been interpreted as representing mid-ocean-ridge style spreading centers (Prockter et al., 2002), to a more complex morphology associated with extension and strike-slip motion (Tufts et al., 1999; Prockter et al., 2000).

Based on cross-cutting relationships between the RS and the bands that comprise the BLC, BLC_3 appears to have formed in conjunction with the RS. A planar reconstruction of this band suggests it formed by some combination of extension and right-lateral, strike-slip motion (Fig. 8c). We have interpreted textural and albedo differences within BLC_3 (inset D of Fig. 8) as indicators that the band may have formed through dextral shear resulting in a series of strike-slip duplexes, perhaps combined with extension. A similar mechanism has been suggested by Prockter et al. (2000) to describe the formation of the band Agenor Linea on Europa. We find no evidence to suggest that compression played a role in the formation of this feature.

Previous planar reconstructions of plates with margins comprised by the RS and BLC (Fig. 9) have suggested that one or both features accommodated compression (Patterson and Pappalardo, 2002; Sarid et al., 2002). Assuming plate rigidity, the application of our modeling technique to plate 4 (Fig. 1b) results in a finite pole of rotation that suggests a reconstruction requiring $\sim$1900 km^2 of surface contraction along the RS (Fig. 11). This reconstruction also bolsters our interpretation that BLC_3 formed, at least in part, through right-lateral strike-slip motion. However, analysis used to test our assumptions about the deformation history of the RS and the rigidity of plates involved in its formation indicates that one or more plates in the region behaved nonrigidly. Furthermore, the magnitude of deformation distributed within one or more of these plates is similar to the offsets of preexisting linear features. It is not clear whether this deformation is associated with a single plate, multiple plates, or distributed amongst all of the plates active during the formation of the RS and BLC_3. Therefore, it remains plausible that plate 4 behaved rigidly and that some component of compression was accommodated at its margins.

5.2. Plate (non)rigidity on Europa

The successful reconstruction of regions involving strike-slip motion and extension on Europa implies that plates can behave rigidly (e.g., Hoppa et al., 2000; Kattenhorn, 2004; Prockter et al., 2002; Schenk and McKinnon, 1989; Tufts et al., 1999, 2000). However, our analysis of a system of plates in the Castalia Macula region with margins consisting of the RS and BLC indicates nonrigid plate behavior occurs. Nonrigid plate behavior has also been inferred by Pappalardo and Sullivan (1996) and Prockter and Pappalardo (2000). It should not be surprising that both rigid and nonrigid plate behavior are present. Nonrigid behavior is commonly associated with predominately rigid plates Earth (see Gordon, 1998 for a review). What is interesting about the nonrigid behavior associated with the plates defined by the RS and BLC is its magnitude.

The best-fit reconstruction of the RS and BLC_3 using ${}_{1*}\mathbf{E}_4$ suggests their formation and/or modification resulted in a $\sim$1% loss of the surface area of plate 4, which represents 1% strain. This reconstruction assumes the plates involved behaved rigidly. However, further analysis using additional approaches to determining ${}_{1}\mathbf{E}_4$, suggests that a component of nonrigid behavior is also present in this plate system. An approximation of the magnitude of that nonrigid behavior indicates it is on par with the rigid component, i.e., the offset created using ${}_{1}\mathbf{D}_4$, is equivalent to the initial offsets of preexisting linear features along the RS. This suggests that an additional $\sim$1% strain associated with the formation and/or modification of the RS and BLC may have been accommodated nonrigidly.

The recognition that nonrigid behavior may play a significant role in shaping the surface of Europa has potential astrobiological implications. The top 1 mm of Europa's water-ice surface is irradiated by interaction with charged particles from Jupiter's magnetosphere producing molecular oxygen, hydrogen peroxide, and other oxidants (Chyba, 2000). Impact gardening results in vertical mixing of these oxidants in the top $\sim$1 m of the surface and protects them from loss by sputtering (Chyba and Phillips, 2001). These oxidants represent a substantial reservoir of biogenic elements and, if available to a subsurface ocean, could potentially support an ecosystem (Chyba and Phillips, 2001). If the surface of Europa behaves rigidly, then pathways for these biogenic elements to reach the subsurface are likely via some form of crustal recycling (e.g., subduction or some other means of balancing the rise of material from the subsurface within extensional bands). However, if the surface of Europa behaves

nonrigidly, then extension could be completely accommodated by means that offer no pathways to for surface produced biogenic elements to reach the subsurface (e.g., folding, internal failure, or ductile flow). This analysis suggests rigid and nonrigid behavior may share equal importance in shaping the surface of Europa.

6. Conclusions

Through detailed analysis of the morphology and cross-cutting relationships of the RS and BLC, we draw the following principal conclusions:

1. The RS represents a single through-going structure that formed in three phases and consists of a collection of ridges that are related spatially and temporally.
2. The offsets of preexisting linear features along the RS suggest a complex deformation history that may result from transpression and/or nonrigid plate behavior.
3. The BLC represents a collection of relatively young bands that formed via extension and strike-slip motion, not a single through-going structure characteristic of convergence.
4. The cross-cutting relationships of the RS and BLC with respect to the surrounding terrain suggest they are related temporally and form the margins of seven plates.

Through inverse modeling of plate motion associated with the formation of the RS and BLC using a technique that we developed, the following additional conclusions were drawn:

5. Nonrigid behavior did play a role in the formation and/or modification of the RS and BLC.
6. The magnitude of nonrigid behavior in this multi-plate system may be equivalent to the magnitude of rigid behavior present.
7. If plate 4 behaved predominately rigidly with respect to the surrounding terrain then its reconstruction suggests that the RS accommodated a component of compression.

Acknowledgements

We would like to thank Donald Forsyth for help in developing our modeling technique and for valuable discussions involving its application. We would also like to thank John Weber and Scott Marshall for helpful reviews provided on the original manuscript. G.W.P. was partially supported for this research by a NASA Graduate Student Research Program Fellowship through the NASA Jet Propulsion Laboratory, which is gratefully acknowledged.

References

Aydin, A., 2006. Failure modes of the lineaments on Jupiter's moon, Europa: implications for the evolution of its icy crust. Journal of Structural Geology, in this issue.

Chase, C.G., 1978. Plate kinematics: the Americas, East Africa, and the rest of the world. Earth and Planetary Science Letters 37, 355–368.

Chyba, C.F., 2000. Energy for microbial life on Europa. Nature 403, 381–382.

Chyba, C.F., Phillips, C.B., 2001. Possible ecosystems and the search for life on Europa. Proceedings of the National Academy of Sciences, USA 98 (3), 801–804.

DeMets, C., Gordon, R.G., Argus, D.F., Stein, S., 1990. Current plate motions. Geophysical Journal International 101, 425–478.

Dixon, T.H., Mao, A., Stein, S., 1996. How rigid is the stable interior of the North American plate? Geophysical Research Letters 21, 3035–3038.

Draper, N., Smith, H., 1981. Applied Regression Analysis, second ed. John Wiley and Sons, New York.

Figueredo, P.H., Greeley, R., 2000. Geologic mapping of the northern leading hemisphere of Europa from Galileo solid-state imaging data. Journal of Geophysical Research – Planets 105, 22,629–22,646.

Figueredo, P.H., Greeley, R., 2004. Resurfacing history of Europa from pole-to-pole geological mapping. Icarus 167, 287–312.

Geissler, P.E., Greenberg, R., Hoppa, G., Helfenstein, P., McEwen, A., Pappalardo, R., Tufts, R., Ockert-Bell, M., Sullivan, R., Greeley, R., Belton, M.J.S., Denk, T., Clark, B., Burns, J., Veverka, J., 1998. Evidence for non-synchronous rotation of Europa. Nature 391, 368–370.

Gordon, R.G., Stein, S., 1992. Global Tectonics and Space Geodesy. Science 256, 333–342.

Gordon, R.G., 1998. The plate tectonic approximation: plate nonrigidity, diffuse plate boundaries, and global plate reconstructions. Annual Review of Earth and Planetary Sciences 26, 615–642.

Greeley, R., Sullivan, R., Klemaszewski, J., Homan, K., Head, J.W., Pappalardo, R.T., Veverka, J., Clark, B.E., Johnson, T.V., Klaasen, K.P., Belton, M., Moore, J., Asphaug, E., Carr, M.H., Neukum, G., Denk, T., Chapman, C.R., Pilcher, C.B., Geissler, P.E., Greenberg, R., Tufts, R., 1998. Europa: initial Galileo geological observations. Icarus 135, 4–24.

Greeley, R., Figueredo, P.H., Williams, D.A., Chuang, F.C., Klemaszewski, J.E., Kadel, S.D., Prockter, L.M., Pappalardo, R.T., Head, J.W., Collins, G.C., Spaun, N.A., Sullivan, R.J., Moore, J.M., Senske, D.A., Tufts, B.R., Johnson, T.V., Belton, M.J.S., Tanaka, K.L., 2000. Geologic mapping of Europa. Journal of Geophysical Research – Planets 105, 22,559–22,578.

Greeley, R., Chyba, C.F., Head, J.W., McCord, T.B., McKinnon, W.B., Pappalardo, R.T., Figueredo, P., 2004. Geology of Europa. In: Bagenal, F., Dowling, T.E., McKinnon, W.B. (Eds.), Jupiter. Cambridge University Press, Cambridge, pp. 329–362.

Greenberg, R., Geissler, P., Hoppa, G., Tufts, B.R., Durda, D.D., Pappalardo, R., Head, J.W., Greeley, R., Sullivan, R., Carr, M.H., 1998. Tectonic processes on Europa: tidal stresses, mechanical response, and visible features. Icarus 135, 64–78.

Greenberg, R., 2004. The evil twin of Agenor: tectonic convergence on Europa. Icarus 167, 313–319.

Greenberg, R., Weidenshilling, S.J., 1984. How fast do Galilean satellites spin? Icarus 58, 186–196.

Head, J.W., Pappalardo, R.T., Sullivan, R., 1999. Europa: morphological characteristics of ridges and triple bands from Galileo data (E4 and E6) and assessment of a linear diapirism model. Journal of Geophysical Research – Planets 104, 24223–24236.

Helfenstein, P., Parmentier, E.M., 1983. Patterns of fracture and tidal stresses on Europa. Icarus 53, 415–430.

Hoppa, G.V., Tufts, B.R., Greenberg, R., Geissler, P.E., 1999a. Formation of cycloidal features on Europa. Science 285, 1899–1902.

Hoppa, G.V., Tufts, B.R., Greenberg, R., Geissler, P.E., 1999b. Strike-slip faults on Europa: global shear patterns driven by tidal stress. Icarus 141, 287–298.

Hoppa, G., Greenberg, R., Tufts, B.R., Geissler, P., Phillips, C., Milazzo, M., 2000. Distribution of strike-slip faults on Europa. Journal of Geophysical Research – Planets 105, 22617–22627.

Hoppa, G.V., Tufts, B.R., Greenberg, R., Hurford, T.A., O'Brien, D.P., Geissler, P.E., 2001. Europa's rate of rotation derived from the tectonic sequence in the Astypalaea region. Icarus 153, 208–213.

Kadel, S., Fagents, S.A., Greeley, R. The Galileo SSI team, 1998. Trough-bounding ridge pairs on Europa – Considerations for an endogenic model of formation, Lunar and Planetary Science Conference XXX [CD-ROM], abstract #1078.

Kattenhorn, S.A., 2004. Strike-slip fault evolution on Europa: evidence from tailcrack geometries. Icarus 172, 582–602.

Kattenhorn, S.A., 2002. Nonsynchronous rotation evidence and fracture history in the Bright Plains region, Europa. Icarus 157, 490–506.

Kogan, M.G., Steblov, G.M., King, R.W., Herring, T.A., Frolov, D.I., Egorov, S.G., Levin, V.Ye., Lerner-Lam, A., Jones, A., 2000. Geodetic constraints on the rigidity and relative motion of Eurasia and North America. Geophysical Research Letters 27, 2041–2044.

Leith, A.C., McKinnon, W.B., 1996. Is there evidence for polar wander on Europa? Icarus 120, 387–398.

Marshall, S.T., Kattenhorn, S.A., 2005. A revised model for cycloid growth mechanics on Europa: evidence from surface morphologies and geometries. Icarus 177, 341–366.

McEwen, A.S., 1986. Tidal reorientation and fracturing of Jupiter's moon Europa. Nature 321, 49–51.

McKenzie, D.P., Parker, R.L., 1967. The North Pacific: an example of tectonics on a sphere. Nature 216, 1276–1280.

Mikhail, G.K., Steblov, G.M., King, R.W., Herring, T.A., Frolov, D.I., Egorov, S.G., Levin, V.Ye., Lerner-Lam, A., Jones, A., 2000. Geodetic constraints on the rigidity and relative motion of Eurasia and North America. Geophysical Research Letters 27, 2041–2044.

Minster, J.B., Jordan, T.H., 1978. Present-day plate motions. Journal of Geophysical Research – Solid Earth 83, 5331–5354.

Moores, E.M., Twiss, R.J., 1995. Tectonics. W.H. Freeman and Company, New York.

Nimmo, F., Gaidos, E., 2002. Strike-slip motion and double ridge formation on Europa. Journal of Geophysical Research – Planets 107, doi:10.1029/2000JE001476.

Ojakangas, G.W., Stevenson, D.J., 1989a. Thermal state of an ice shell on Europa. Icarus 81, 220–241.

Ojakangas, G.W., Stevenson, D.J., 1989b. Polar wander of an ice shell on Europa. Icarus 81, 242–270.

Pappalardo, R.T., Sullivan, R.J., 1996. Evidence for separation across a gray band on Europa. Icarus 123, 557–567.

Patterson, G.W., Pappalardo, R.T., 2002. Compression across ridges on Europa. 34th Lunar and Planetary Science Conference Abstracts, 1681.

Prockter, L.M., Antman, A.M., Pappalardo, R.T., Head, J.W., Collins, G.C., 1999. Europa: stratigraphy and geological history of the anti-Jovian region from Galileo E14 solid-state imaging data. Journal of Geophysical Research – Planets 104, 16,531–16,540.

Prockter, L.M., Pappalardo, R.T., Head, J.W., 2000a. Strike-slip duplexing on Jupiter's icy moon Europa. Journal of Geophysical Research – Planets 105, 9483–9488.

Prockter, L.M., Pappalardo, R.T., 2000b. Folds on Europa: implications for crustal cycling and accommodation of extension. Science 289, 941–943.

Prockter, L.M., Head, J.W., Pappalardo, R.T., Sullivan, R.J., Clifton, A.E., Giese, B., Wagner, R., Neukum, G., 2002. Morphology of Europan bands at high resolution: a mid-ocean ridge-type rift mechanism. Journal of Geophysical Research – Planets 107, doi:10.1029/2000JE001458.

Sarid, A.R., Greenberg, R., Hoppa, G.V., Hurford, T.A., Tufts, B.R., Geissler, P., 2002. Polar wander and surface convergence of Europa's ice shell: evidence from a survey of strike-slip displacement. Icarus 158, 24–41.

Schenk, P.M., McKinnon, W.B., 1989. Fault offsets and lateral crustal movement on Europa: evidence for a mobile ice shell. Icarus 79, 75–100.

Schulson, E.M., 2002. On the origin of a wedge crack within the icy crust of Europa. Journal of Geophysical Research – Planets 107, doi:10.1029/2001JE001586.

Sella, G.F., Dixon, T.H., Mao, A., 2002. REVEL: a model for recent plate velocities from space geodesy. Journal of Geophysical Research – Solid Earth 107, doi:10.1029/2000JB000033.

Sullivan, R., Greeley, R., Homan, K., Klemaszewski, J., Belton, M.J.S., Carr, M.H., Chapman, C.R., Tufts, R., Head, J.W., Pappalardo, R., Moore, J., Thomas, P., 1998. Episodic plate separation and fracture infill on the surface of Europa. Nature 391, 371–373.

Tufts, B.R., Greenberg, R., Hoppa, G., Geissler, P., 1999. Astypalaea Linea: A large-scale strike-slip fault on Europa. Icarus 141, 53–64.

Tufts, B.R., Greenberg, R., Hoppa, G., Geissler, P., 2000. Lithospheric dilation on Europa. Icarus 146, 75–97.

Turtle, E.P., Melosh, H.J., Phillips, C.B., 1998. Tectonic modeling of the formation of Europan ridges. Eos Transaction, AGU 79 (45) (Fall Meeting Supplement, F541).